CHALMERS
UNIVERSITY OF TECHNOLOGY

X-ray simulations with gVXR in education, digital twining, experiment planning, and data analysis

Downloaded from: https://research.chalmers.se, 2025-12-06 16:34 UTC

Citation for the original published paper (version of record):
Vidal, F., Afshari, S., Ahmed, S. et al (2025). X-ray simulations with gVXR in education, digital twining, experiment planning, and data
analysis. Nuclear Instruments and Methods in Physics Research, Section B: Beam Interactions with Materials and Atoms, 568. http://dx.doi.org/10.1016/j.nimb.2025.165804

N.B. When citing this work, cite the original published paper.

research.chalmers.se offers the possibility of retrieving research publications produced at Chalmers University of Technology. It covers all kind of research output: articles, dissertations, conference papers, reports etc. since 2004. research.chalmers.se is administrated and maintained by Chalmers Library

(article starts on next page)

Nuclear Inst. and Methods in Physics Research, B 568 (2025) 165804

Contents lists available at ScienceDirect

Nuclear Inst. and Methods in Physics Research, B

journal homepage: www.elsevier.com/locate/nimb

Full Length Article

X-ray simulations with gVXR in education, digital twining, experiment planning, and data analysis

Franck P. Vidal [1,2,*], Shaghayegh Afshari [3], Sharif Ahmed [4], Alberto Albiol [5], Francisco Albiol [6], Éric Béchet [7], Alberto Corbí Bellot [8], Stefan Bosse [9,10], Simon Burkhard [11], Younes Chahid [12], Cheng-Ying Chou [3], Robert Culver [13], Pascal Desbarats [14], Lewis Dixon [2], Johan Friemann [15], Amin Garbout [16], Marcos García-Lorenzo [17], Jean-François Giovannelli [18], Ross Hanna [13], Clémentine Hatton [19], Audrey Henry [19], Graham Kelly [20], Christophe Leblanc [7], Alberto Leonardi [4], Jean Michel Létang [21], Harry Lipscomb [16], Tristan Manchester [4], Bas Meere [22], Claire Michelet [23], Simon Middleburgh [2], Radu P. Mihail [24], Iwan Mitchell [2], Liam Perera [4], Martí Puig [16,25], Malek Racy [26], Ali Rouwane [23], Hervé Seznec [23], Aaron Sújar [17], Jenna Tugwell-Allsup [27], Pierre-Frédéric Villard [28]

[1] *UKRI-STFC Scientific Computing, Daresbury Laboratory, UK*
[2] *School of Computer Science & Engineering, Bangor University, UK*
[3] *Department of Biomechatronics Engineering, National Taiwan University, Taiwan*
[4] *Diamond Light Source, UK*
[5] *PRHLT Research centre, Universitat Politècnica València, Spain*
[6] *Instituto de Física Corpuscular, CSIC-Universitat de València, Spain*
[7] *Département d'Aérospatiale et Mécanique, Université de Liège, Belgium*
[8] *Escuela Superior de Ingeniería y Tecnología - Universidad Internacional de La Rioja, Spain*
[9] *Department of Computer Science, University of Koblenz, Germany*
[10] *Department of Mechanical Engineering, University of Siegen, Germany*
[11] *Federal Institute of Metrology METAS, Bern-Wabern, Switzerland*
[12] *UK Astronomy Technology Centre, Royal Observatory, UK*
[13] *The Manufacturing Technology Centre, UK*
[14] *Univ. Bordeaux, CNRS, Bordeaux INP, LaBRI, UMR 5800, France*
[15] *Department of Industrial and Materials Science, Chalmers University of Technology, Sweden*
[16] *Henry Royce Institute, Henry Moseley X-ray Imaging Facility, Department of Materials, The University of Manchester, UK*
[17] *Grupo de Modelado y Realidad Virtual, Universidad Rey Juan Carlos, Spain*
[18] *Univ. Bordeaux, CNRS, Bordeaux INP, IMS, UMR 5218, France*
[19] *Scalian DS, France*
[20] *Shrewsbury and Telford Hospital NHS Trust, UK*
[21] *INSA-Lyon, Université Claude Bernard Lyon 1, CNRS, Inserm, CREATIS UMR 5220 U1294, France*
[22] *Department of Mechanical Engineering, Eindhoven University of Technology, Netherlands*
[23] *Univ. Bordeaux, CNRS, LP2I Bordeaux, UMR 5797, France*
[24] *Department of Computer Science and Engineering Technology, Valdosta State University, USA*
[25] *Department of Engineering Science, University of Oxford, UK*
[26] *Salford Royal Hospital, Manchester, UK*
[27] *Radiology Department, Betsi Cadwaladr University Health Board (BCUHB), Ysbyty Gwynedd, UK*
[28] *Université de Lorraine, CNRS, Inria, LORIA, France*

ARTICLE INFO

Keywords:
X-ray imaging
Computed tomography
Simulation
GPU programming

ABSTRACT

gVirtualXray (gVXR) is an open-source framework that relies on the Beer–Lambert law to simulate X-ray images in real time on a graphics processor unit (GPU) using triangular meshes. A wide range of programming languages is supported (C/C++, Python, R, Ruby, Tcl, C#, Java, and GNU Octave). Simulations generated with gVXR have been benchmarked with clinically realistic phantoms (i.e. complex structures and materials) using Monte Carlo (MC) simulations, real radiographs and real digitally reconstructed radiographs (DRRs),

* Corresponding author at: UKRI-STFC Scientific Computing, Daresbury Laboratory, UK.
E-mail address: franck.vidal@stfc.ac.uk (F.P. Vidal).

https://doi.org/10.1016/j.nimb.2025.165804

Available online 28 August 2025
0168-583X/© 2025 The Authors. Published by Elsevier B.V. This is an open access article under the CC BY license (http://creativecommons.org/licenses/by/4.0/).

Digital twinning
Registration
Machine learning

and X-ray computed tomography (CT). It has been used in a wide range of applications, including real-time medical simulators, proposing a new densitometric radiographic modality in clinical imaging, studying noise removal techniques in fluoroscopy, teaching particle physics and X-ray imaging to undergraduate students in engineering, and XCT to masters students, predicting image quality and artifacts in material science, etc. gVXR has also been used to produce a high number of realistic simulated images in optimisation problems and to train machine learning algorithms. This paper presents a comprehensive review of such applications of gVXR.

1. Introduction

The simulation of accurate and fast X-ray images remains a challenge. State-of-the-art Monte Carlo (MC) methods can mimic the physics, by tracking photons as they travel from the source, through matter, to the detector. The computational cost makes it prohibitive in many applications where speed is a requirement, e.g. interactive virtual reality (VR) or high data throughput support. However, it is possible to trade off some of the physical effects such as scattering to speed-up computations, whilst retaining a high level of accuracy.

In Section 2, we describe an open-source framework called gVirtualXray (gVXR). No proprietary technology is used, making it portable and deployable on a wide range of hardware and software platforms. gVXR implements a deterministic simulation model based on the Beer–Lambert law to generate noise-free images. They can provide a good compromise between speed and accuracy [1] and can be implemented on graphics processor units (GPUs) for a further increase of speed [2,3]. Unlike Monte Carlo methods, deterministic simulations tend to ignore scattering and noise. In gVXR, the latter is added as a post-process. The software has been quantitatively tested and validated against MC and experimental data (Section 3). Remaining sections show how it has been deployed in a broad range of applications in various scientific contexts.

gVXR was initially used for training purposes (Section 4). Three approaches have been followed: immersive virtual environments (Section 4.1), graphical user interface (GUI) desktop applications (Section 4.2), and programming-based learning (Section 4.3).

In recent years, attention has shifted towards the digital twining of real file systems (Section 5) and by extension high-throughput data applications where it excels compared to MC methods, e.g. machine learning (Section 9) and mathematical optimisation (Section 10).

Section 5 shows examples for laboratory computed tomography (labCT) devices (Sections 5.1 and 5.2) as well as a synchrotron beamline (Section 5.3). The aim is to finely tweak the parameters of the simulation to generate synthetic data representative of a specific device. Digital twins can be integrated in our web-based application (Section 5.4).

With the possibility to generate realistic images tuned for specific devices, it became possible to perform virtual experiments, conduct feasibility studies, and optimise the scanning parameters for real experiments (Section 6.1), or even to fuse simulated data with experimental data to improve the contrast in clinical densitometric images (Section 6.2). gVXR has been used to generate ground-truth complete and incomplete datasets to conduct quantitative studies and assess the accuracy of iterative computed tomography (CT) reconstruction algorithms (Section 7).

In addition, motion blur can be added to enhance the simulation model when the source/detector or sample/patient are moving during the acquisition of a radiograph (Section 8). It has been used to test the feasibility of non-destructive testing (NDT) of the blades of wind turbines (Section 8.1) and to add respiration artefacts in synthetic cone-beam computed tomography (CBCT) data (Section 8.2).

The use of gVXR is increasing in machine learning applications. Early applications dating back to 2016 are briefly reviewed in Section 9.1. A popular approach is data augmentation for image segmentation (Section 9.2). It has been used for lung nodule detection in two-dimensional (2D) radiographs (Section 9.2.1), woven carbon fibre reinforced woven composites (Section 9.2.2), and material decomposition using spectral CT data (Section 9.2.3). Section 9.3 details how gVXR was integrated in a complex pipeline to detect and characterise defects in homogeneous aluminium die casting plates and composite fibre-metal laminate plates (Section 9.3.1), and characterise the internal surface roughness in additive manufacturing (Section 9.3.2).

When used in mathematical optimisation, gVXR generates a huge amount of images that are typically compared with experimental data to minimise an objective function (Section 10). It has been used medical imaging for 3D-to-2D registration to deform a generic three-dimensional (3D) hand model so that its radiograph matches a clinical radiograph (Section 10.1). An experimental synchrotron X-ray micro-CT dataset corrupted by strong artefacts was accurately reproduced by simulation (Section 10.2). It made it possible to extract feature sizes and positions, which proved to be nearly impossible otherwise. Section 10.3 demonstrates how to finely assess the focal spot shape and restore image quality in blurred images. Section 10.4 demonstrates that it is possible to compare a manufactured object with its original computer-aided design (CAD) model, and visualise and quantify discrepancies. The last application presented in the paper describes in Section 10.5 how gVXR is deployed to automatically tune the geometry of a CT scan acquisition to maximise the visibility of small defects in critical parts of aerofoil blade component.

The paper ends with conclusions in Section 11.

2. Description

gVXR is an open-source application programming interface (API) written in C++ to compute the Beer–Lambert law, also known as the attenuation law. If scattering is neglected and an ideal (i.e. Dirac) point-spread function is assumed, X-ray projections $\mathbf{I}(x, y)$ can simply be modelled with the Beer–Lambert attenuation law:

$$\mathbf{I}(x, y) = \sum_i \mathbf{R}(E_i)\,\mathbf{D}(E_i)\,\exp\left(-\sum_j \mu_j(E_i)\,\mathbf{d}_j(x, y)\right) \tag{1}$$

$\mathbf{I}(x, y)$ is the integrated energy in electronvolt (eV), kiloelectronvolt (keV) or megaelectronvolt (MeV), units of energy commonly used in atomic and nuclear physics, received by pixel (x, y). The beam spectrum emitted by the X-ray source is discretised in several energy channels in the polychromatic case. E_i corresponds to the energy of the ith energy channel. $\mathbf{D}(E_i)$ is the number of photons emitted by the source at that energy E_i. When the source is monochromatic, e.g. in the case of synchrotron radiation, a single energy channel is used. The detector response $\mathbf{R}(E_i)$ mimics the use of a scintillator. It is implemented as a lookup table to replace the incident energy E_i with a smaller value, i.e. $\mathbf{R}(E_i) < E_i$. Absorption edges of the elements that make up the scintillator (escape effects) are taken into account when building the lookup table. The detector response is assumed space-invariant in Eq. (1). j indicates the jth material being scanned when a multi-material "object" is considered. $\mu_j(E_i)$ is the linear attenuation coefficient in cm^{-1} of the jth material at energy E_i. $\mathbf{d}_j(x, y)$ is the path length in cm of the ray from the X-ray source to pixel (x, y) crossing the jth material.

Polygon meshes, e.g. triangles, are used in gVXR to represent 3D objects. This method is commonly used in computer graphics (CG), including real-time video games and VR, animations, and CAD. It is intuitive to compute the Beer–Lambert law with ray-tracing when polygon meshes are used. However, this technique is relatively computationally intensive: (i) a ray must be fired between the source and each

detector pixel, and (ii) intersection tests for each ray for each triangle of each 3D object must be performed. Freud et al. adapted the Z-buffer technique to efficiently compute $\mathbf{d}_j$ in Eq. (1) from polygon meshes [4]. It relies on rasterisation and does not require to sort intersections. In this case, each polygon is processed a single time, projecting it on the detector plane, and using an accumulator buffer. The computational complexity is considerably reduced.

gVXR implements Freud's algorithm on GPU using a graphics API [2]. Since its inception, functionalities have been added to gVXR to improve the level of realism of the simulations. A monochromatic source was initially used to mimic fluoroscopy in a real-time medical VR simulator [5]. Polychromatism and the focal spot of the detector were then introduced to improve realism [6]. In 2013, the code was redeveloped to become, gVXR, and was made available to the community as an open-source project on SourceForge (https://sourceforge.net/projects/gvirtualxray/, accessed: 18 Jul 2024) [3]. The impulse response of the detector and Poisson noise are also supported [7]. The scintillator material of the detector and the tube voltage and beam filtration can now be specified [8].

gVXR is cross-platform: it runs on Windows, GNU/Linux, and MacOS computers (Intel architecture only, although ARM support is planned). It supports GPUs from any manufacturer. gVXR is scalable: it runs on laptops, desktop PCs, supercomputers, and cloud infrastructures. Containerisation using Docker is even possible [9]. A wide range of programming languages (C/C++, Python, R, Ruby, Tcl, C#, Java, and GNU Octave) can be used. Its Python package is available on the Python Package Index (https://pypi.org/project/gVXR/, accessed: 18 Jul 2024).

Surface meshes (triangles) in most popular file formats (e.g. STL, PLY, 3DS, OBJ, DXF, X3D, DAE) can be used to define the geometry of scanned objects. Volume meshes (tetrahedrons) in the Abacus format may also be used but their support is experimental. The material property must be specified for each scanned object. Chemical elements (e.g. the symbol 'W' or the atomic number 74 for tungsten); compounds, e.g. H_2O for water; mixtures, e.g. Titanium-aluminium-vanadium alloy, Ti90Al6V4; and Hounsfield units (for medical applications) are supported. The photon cross-sections provided by Xraylib [10] (https://github.com/tschoonj/xraylib, accessed: 18 Jul 2024) are used to compute μ values in Eq. (1).

Cone beam geometries (both point sources and focal spots) are supported to mimic X-ray tubes. A parallel beam can be used for synchrotrons. The beam spectrum can be either monochromatic or polychromatic. Both SpekPy [11] and Xpecgen [12] are supported as backends to specify the tube voltage and the beam filtration used. To increase realism, photonic noise can be turned on. In this case, the photon flux must be specified. Gao et al. recently exploited gVXR to investigate the impact of the properties of the X-ray source, detectors, and scanned object in X-ray images for material science [13]. In a metrology application, where national standards are established and an ISO standard in preparation, Ou et al. studied how the CT imaging system parameters can influence "type A" standard uncertainty [14]. In a clinical application, Scarponi et al. used these features to conduct a validation study of a virtual augmentation of fluoroscopic images during endovascular interventions [15].

It is possible to model ideal detectors as well as realistic detectors. In this case, the user can specify a point spread function (PSF), i.e. the level of blur inherent to the detector, and the thickness and material composition of the scintillator. It is also possible to simulate spectral imaging.

Orbital, helical and arbitrary trajectories can be supported to simulate a CT acquisition. It is possible to describe the simulation and CT acquisition in Python (or any other supported programming languages) or using a user-friendly JSON file that is loaded from the Python code. Full examples of CT simulation with gVXR and CT reconstruction with the Core Imaging Library (CIL) [16] are available as Jupyter notebooks on GitHub (https://github.com/TomographicImaging/gVXR-Tutorials).

3. Validation

To validate the accuracy of gVXR, successive validation tests of increasing complexity were performed. Each milestone was validated individually with an appropriate methodology. For the Beer–Lambert implementation, we initially compared simple images simulated with gVXR with corresponding images simulated with a state-of-the-art Monte Carlo package (Geant4/Gate) [3].

More advanced functionalities, such as voltage, beam filtration and scintillation, were validated using two anthropomorphic phantoms. The first one is a digital phantom: pEdiatRic dosimetRy personalized platfORm (ERROR) [17]. It corresponds to the anatomy of a 5-year-old boy. It is provided as a labelled $512 \times 511 \times 190$ volume, which includes 24 different structures, such as air, muscle, bone, stomach-interior, cartilage, etc. As it is a digital phantom, it can be used to compare gVXR and Gate's simulations. The number of photons impinging the detector was 10^9. About 10 days of computations were required on the test computer to produce a simulated image of 128×128 pixels with Gate; only a few microseconds gVXR. Both simulations are visually close. All the image comparison metrics indicate that the images are extremely similar when scattering is ignored: Zero-mean normalised cross-correlation (ZNCC) is 99.99%, which is close to the optimal 100% value; mean absolute percentage error (MAPE) is 2.23%, which is close to 0%; and structural similarity index (SSIM) is 0.99, which is close to 1.

The second phantom is the Lungman anthropomorphic chest phantom (Kyoto Kagaku, Tokyo, Japan) [18]. It represents a 70 kg male. The phantom is made of materials with X-ray absorption properties close to those of human tissue. Tumors of various densities are embedded. A CT scan of the phantom was acquired with a device clinically utilised at Ysbyty Gwynedd Hospital (UK), a 128-slice Somatom Definition Edge scanner by Siemens Healthcare (Erlangen, Germany). A digital phantom was first created by image segmentation using open-source toolkits, the Insight Toolkit (ITK) [19] and Visualization Toolkit (VTK) [20]. The digital phantom is freely available on Zenodo [21]. The material composition of each segmented structure is derived from the average Hounsfiled unit of the structure in the original CT scan. Schneider et al. [22]'s method is built in gVXR to convert the Hounsfield values into material compositions and densities. A CT scan acquisition is then simulated using gVXR and reconstructed with CIL [16]. The original CT scan taken with the Somatom Definition Edge scanner can be compared with CT volume reconstructed from simulated data. Corresponding slices are close to each other. Hounsfield values are comparable. MAPE is about 5% and the ZNCC is above 98%, indicating a high level of correlation between the two volumes. The errors are more due to segmentation inaccuracies and noise than the simulation implementation itself. Indeed, when simulated X-ray projections are compared with digitally reconstructed radiographs (DRRs) computed from the experimental CT scan, ZNCC is 99.66%, SSIM is 0.98, and MAPE is 1.76%.

gVXR is so fast that it is possible to embed the X-ray simulation into objective functions and register a simulated radiograph on experimental data (see Fig. 44). A real digital radiograph was taken with a clinical X-ray machine by GE Healthcare (Chicago, Illinois, USA) at Ysbyty Gwynedd Hospital. The digital Lungman phantom was registered to reproduce the same position and orientation as in the digital radiography taken with the clinical device. ZNCC is 98.91%, SSIM is 0.94, and MAPE is 1.56%. It demonstrates the ability of gVXR to reproduce radiographs taken with clinically utilised devices.

4. Education

The use of simulation in the curriculum has numerous benefits for both clinical [23] and industrial radiography. Simulation can avoid several risks and provide realistic experiences in areas where there are limited opportunities for direct access to specialised equipment [24]. It

permits trainees to familiarise themselves to systems without the risk of damaging expensive operational instruments. In labCT for example, detectors can be damaged by crashing samples into them or saturation, with detectors costing over £50,000 each.

However, care must be given to provide high-fidelity simulations as inaccurate representation can lead to the inaccurate transferability into practice, causing risks involving ionising radiation. This is particularly true in clinical radiology, where patients, carers and staff are present and with legal requirements governing practices [25]. As per these regulations, ionising radiation should be kept as low as reasonably practical, with students having to be directly supervised with no room for errors and flexibility in practice. Due to limited placement opportunities and workforce capacity issues to train, the use of simulation is also increasing and evolving in education to create capacity and flexibility in gaining required clinical skills differently. In addition, some imaging examinations are rarely performed or are only performed in specialised centers, so simulation allows such examinations to be replicated to develop some experience in their acquisition. Demonstrating how image quality and radiation dose is influenced by modifications in acquisition parameters (e.g. kilovoltage peak (kVp), milliampere-second (mAs)) on equipment is extremely valuable in gaining a richer understanding of radiographic practices. Again, this is particularly important in clinical practice, due to the harmful effects of ionising radiation, we are limited to how we can test our radiographic practices as it is unethical to use patients. For the same reason, caution may also be required with samples. A high radiation dose can damage samples, e.g. by creating cracks in their structures. Placement experience can only provide certain scenarios due to variability of daily activities, whereas simulation can provide complex, different scenarios to enhance the learning experience. The same benefits are also applicable to industrial radiography as samples will vary a lot from one user to another. Allowing modification of parameters and multiple exposures is obviously not unethical in this case; however, it enables operators to select suitable parameters by trial and error much more efficiently.

4.1. Virtual environments

gVXR's predecessor was initially used in-house for medical training using VR. Villard et al. used gVXR's predecessor to implement a simulator for interventional radiology, focusing on percutaneous transhepatic cholangiography (PTC) [5]. This procedure consists of inserting a needle into the biliary tree using fluoroscopy (real-time X-ray imaging) for guidance. A hybrid computing approach was adopted. The respiration of the virtual patient and the needle force feedback were performed on central processor unit (CPU), whilst the fluoroscopy was performed on GPU. The respiration and fluoroscopy simulations were tunable to account for patient variability. Once the implementation became opensource, Zuo et al. developed a catheterisation and angiography positioning simulation [26]. A mixed reality application for veterinary medicine was recently reported [27]. It has been implemented using the Unity® 3D game engine.

4.1.1. Haptic femoral nailing simulator

gVXR was applied effectively in the development of a VR haptic orthopedic surgical simulator [28]. Orthopedic surgery requires three-dimensional surgical tool triangulation, referenced largely from static orthogonal fluoroscopy images taken intraoperatively. One such procedure is intramedullary nailing for femoral fractures, where the procedure is undertaken through relatively minimal skin incisions, using tactile feedback of the tools on bone and static 2-dimensional image intensifier guidance. Effective and realistic image intensifier functionality is therefore critical for the functionality of such a simulator. The simulator was built using Unreal Engine (Epic Games Inc., Cary, North Carolina), an advanced 3D game development engine, free for non-commercial use. The gVirtualXray plugin was adapted for use within this engine by Toia Ltd (https://toia.tech/) who also provided haptic and 3D environment support for the project. Interaction was via a VR headset with full head position tracking and a 3D printed drill handle attached to a haptic device. The virtual image intensifier was controlled by a separate user to simulate the necessary intraoperative communication, image interpretation and non-technical skills (see Fig. 1(a)). The virtual X-ray source was placed at the corresponding location on the virtual image intensifier. The output from the ray tracing image needed to be converted from a continuous video stream to still images, as orthopedic procedures use static images to limit the radiation exposure to the patient and staff. To avoid the need for editing the plugin, this was carried out using a camera relay system, where the video output was displayed on a virtual screen outside the view of the user. A camera was placed in front of this screen and could be controlled to take still images which were then displayed on the corresponding screens of the image intensifier, allowing images to be 'saved' for later reference whilst the c-arm screening position changed (see Fig. 1(b)). The objects within the path were assigned values to customise their attenuation of the virtual X-ray beam and recreate the visual appearance of bone, metalwork and soft tissues. The simulator was validated in a study involving orthopedic surgeons and trainees, where the quality, accuracy and realism of the image intensifier functionality was highly rated by the majority of users.

4.1.2. LabCT in a game engine

gVXR was embedded in the Unreal Engine 5, a very popular game engine developed by Epic Games, as there is relatively little education or training material available for introducing members of the public, academics or operators to labCT [29]. The user evolves in a 3D virtual environment with a labCT scanner (see Fig. 2). The user can interact with this in a very similar way to how they would in real life, including procedures such as correctly positioning samples, choosing beam energy and performing simple image analysis. The application also provides an interface for gVXR library without the need for the user to understand how to use the command line. Following its development, the application was submitted to several experts in the field of labCT, some of whom had previous experience with using game engines in their work. The consensus was that the application was relatively usable, scoring above 60 points in a system usability survey, and feedback was generally positive about the ease of use, features provided and similarities with working with real hardware.

4.2. Interactive teaching tool for medical radiography

In clinical radiography, trainees must learn how to produce the best image whilst reducing the radiation dose to the minimum requirement. Projectional radiography is still usually taught in a traditional way, i.e. through lectures and practical sessions within the university and clinical settings using an X-ray full body phantom. The information learned in the lectures is based on books and files containing static content from academic or hospital databases. It is therefore not possible to observe the effect of acquisition parameters on the images. Another important aspect is patient positioning, which cannot be easily learned from the final static resultant images. Mistakes are also key aspects of the learning process and it is important for trainees to learn from them to make sure they are not replicated in the clinical setting. However, with static images, they do not have the opportunity to modify the device's settings and cannot practice with the patients' positioning in a live and dynamic process. Practicals in a clinical setting is not problem-free, as the practice of the techniques learned and the effects of the physical principles cannot be trained freely due to the risks of exposure of living tissues to radiation. gVirtualXRay and 3D character animation have been integrated into a medical teaching tool (see Fig. 3) to allow real-time acquisition of images of anatomically realistic virtual patients [30]. The user can interactively change the device parameters and patient positioning, and visualise the resulting radiograph in real time in a 3D virtual environment. A face and content validation study

(a) The virtual operating theater, as viewed through the VR headset. The virtual X-ray source is placed on the corresponding location on the c-arm (asterisk). Final images are displayed on the image intensifier screen (arrow).

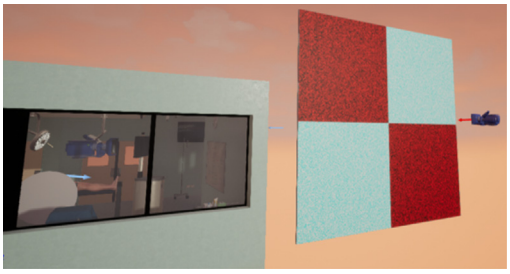

(b) The camera relay system. The virtual X-ray images are displayed on a screen outside the field of view of the user, with a separate camera used to take still images for display on the image intensifier screen (see arrow in Figure 1a).

Fig. 1. Screenshots of the haptic femoral nailing simulator.

Fig. 2. Video 1 – Virtual environment featuring a labCT device powered by gVXR and the Unreal Engine. https://youtu.be/_hFx7rln09k?.

showed that the software was realistic, useful and suitable for teaching X-ray radiography. Utilising this technology can help reduce active clinical training in a busy X-ray room environment, which can help ensure clinical patient flow and efficiency is maintained. Students receive a supplemented virtual clinical education which will better prepare them for real clinical situations.

4.3. Programming approaches

4.3.1. Online virtual laboratories using Docker

Often, online teaching makes use of overly simplistic applet-based simulations that strip down the reality of complex radiation/matter interactions. It can lead to a disconnection between the teaching material and the current scientific environments and engineering settings. To address this deficiency, gVirtualXray and other state-of-the-art simulation tools such as Geant4 [31] are integrated to offer an online collaborative laboratory dedicated to X-ray imaging (see Figs. 4) [9]. It is aimed at distance learning mature (37 years old or above) undergraduate students in engineering at Universidad Internacional de La Rioja (UNIR) in Spain. A collaborative programming interface and 3D visualisation tools are provided to complete hands-on activities (see Fig. 5). This way students can specify the parameters of their simulations and "see" the corresponding results. The online virtual laboratory relies on modern computing techniques such as virtualisation, cloud infrastructures, containers, networking and shared collaboration environments. Almost all the activities can be used in a web browser thanks to free cloud services. This approach (virtualisation and cloud computing) removes the need for complex software deployments. It has proven (over a period of several academic terms) to be both very attractive to and pedagogically successful (technically, and scientifically) for online engineering undergraduates.

4.3.2. In-person training using JupyterLab

We have deployed gVXR in material science lab-sessions delivered to about 150 Master of Engineering (MEng) students a year at the INSA-Lyon and Polytech Lyon 1 engineer schools. It has been embedded in a Jupyter notebook together with the open-source reconstruction toolkit RTK [32]. Several interactive exercises have been proposed to enable students to learn and gain hands-on experience with X-ray tomographic setups. They first study both digitally with the twin and experimentally with the bench the critical sensibility to crack orientation in a cylindrical sample (additive manufacturing) in which a through crack has been added. Then the students gradually familiarise themselves with the 3D reconstruction technique: (i) first with mono-energy and no noise (i.e. infinite stat), then (ii) with a given exposure (i.e. number of X-rays per pixel) to highlight photon starvation, and (iii) finally

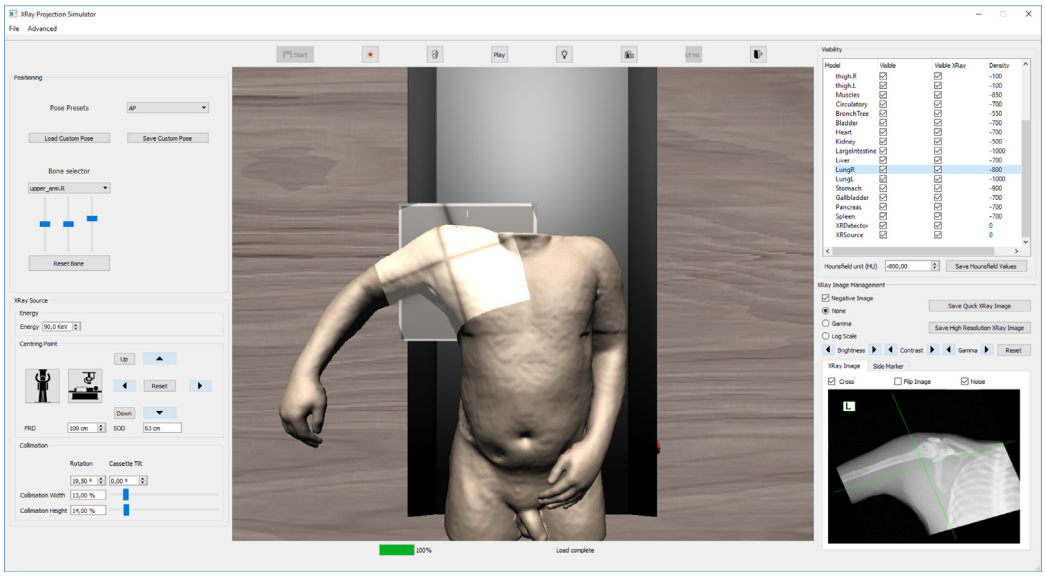

Fig. 3. Video 2 – Interface of the Projectional Radiography Simulator. Combining gVirtualXRay and an interactive character animation method, users are able to practice posing and getting patient's images in real-time. https://www.youtube.com/watch?v=WFOAVSLXufs.

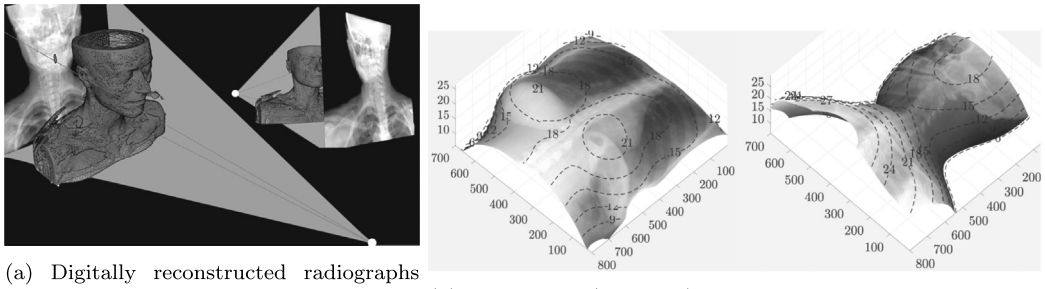

(a) Digitally reconstructed radiographs and corresponding 3D visualisations in gVXR.

(b) Path length (L-buffers) represented as 3D shapes with the corresponding X-ray radiograph projected onto them.

Fig. 4. Examples of containerised simulations performed using gVirtualXray.

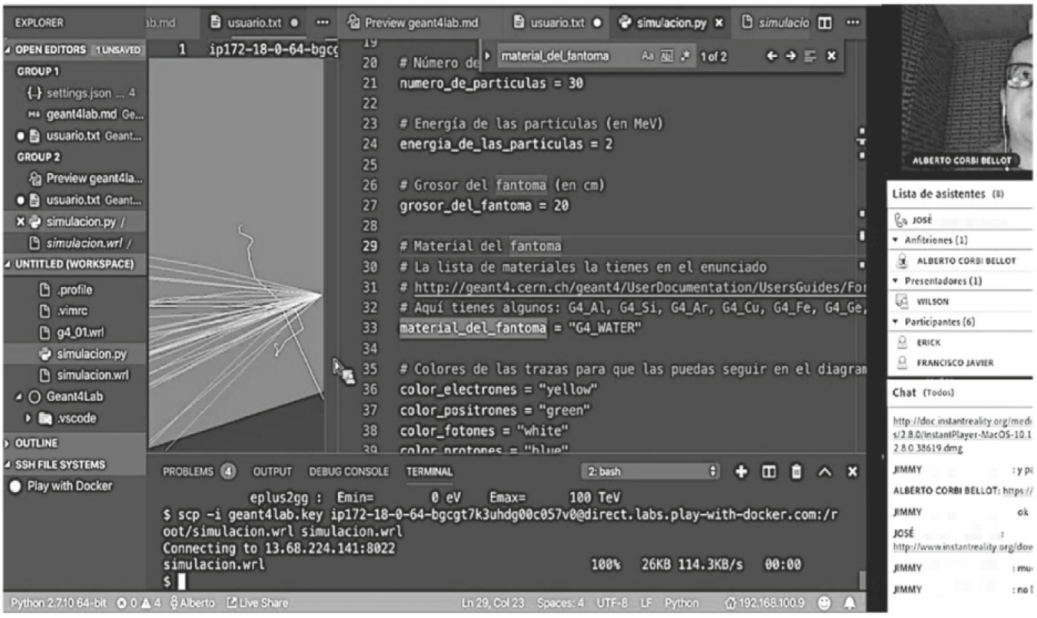

Fig. 5. Example of collaborative programming session on Geant4.

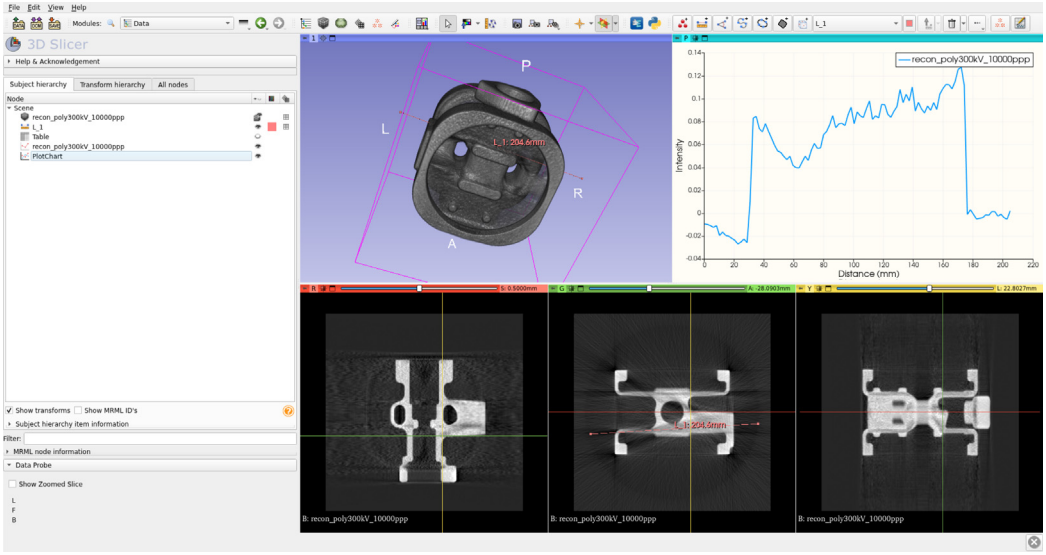

Fig. 6. Example of visualisation (3D-Slicer) of a reconstructed gVXR-simulated volume of an industrial part: volume rendering, sampled profile in the volume and orthogonal sections.

with a realistic energy distribution typical of an X-ray generator to understand beam hardening. An example of the 3D visualisation of the reconstructed simulated volume is shown in Fig. 6. It is worth noting that this progression in the complexity of the imaging setup cannot be done experimentally with such cohort sizes. The digital twinning of the X-ray setup is crucial for those lab sessions of the material science department.

5. Digital twinning

Digital Twinning is the creation of virtual models of real-life components. In this case, gVirtualXray allows true representative X-ray simulations calibrated to real-life machines. To create a Digital Twin, all factors of an X-ray system must be taken into account, ranging from the mechanics of the system (can the detector or source move? What clearance is available for the sample?, etc.) to X-ray source and detector properties (maximum voltage, focal spot size, pixel resolution, scintillator properties, PSF, and so forth). A core part of creating a Digital Twin is calibrating the noise of a system based on the target amperage, this involves an experimental method to measure the noise characteristics at differing mAs values, which then can be exposed in the model as a parameter to users of the Virtual Twin.

The development of such digital twins opens up new perspectives, it is now possible:

- To train users on specific devices;
- To predict what experimental data will look like from CAD models;
- To assess the feasibility of scanning specific samples on specific devices before submitting beamtime proposals to facilities;
- To optimise scanning parameters offline, i.e. before beamtime;
- To generate a large amount of automatically annotated data for training machine learning algorithms;
- To design new systems.

5.1. Dedicated models

The interaction of a scintillator detector with a continuous X-ray spectrum is non-trivial and has an influence on the signal-to-noise ratio of an X-ray projection image. For making an X-ray projection simulation as realistic as possible for a specific setup, it therefore helps to be able to include a model of this particular detector in the simulation process. While X-ray simulation tools commonly include some form of detector model that can be parametrised, full flexibility in applying any type of detector model is only given if the geometric part (ray-tracing) and the signal generation (interaction of the incident spectrum with the detector) can be separated. It is possible to use generic models built in gVXR to specify the scintillator material and thickness, and photon flux. However, gVXR also offers the functionality of calculating only the pixel-resolved path length of X-rays passing through a simulation object without conversion to a gray value projection image, leaving the detector interaction entirely to the user. Combined with the Python interface, this provides us an efficient way of verifying our measurement-based detector models in simulations by comparing with measured projection data. To validate the approach, we recorded and simulated 16 identical projections of a titanium step wedge imaged with 120 kV tube voltage and 0.03 mm aluminium pre-filter. For every pixel, the average (see Fig. 7) and the variance (see Fig. 8) of the gray value across the 16 projections are calculated.

(a) Experimental. (b) Simulated.

Fig. 7. Average images computed from 16 identical noisy projections of a titanium step wedge imaged with 120 kV tube voltage and 0.03 mm Al pre-filter.

Fig. 7 shows that the average gray scale values over 16 noisy experimental and 16 noisy simulated projections seem to be visually similar, whilst Fig. 8 shows that the noise levels seem to be too. It is possible to assess the relationship between gray scale value and standard deviation. The plots in Fig. 9 shows that the specific detector and noise models implemented on top of gVXR are able to generate images that are realistic with respect to those produced with our XCT device.

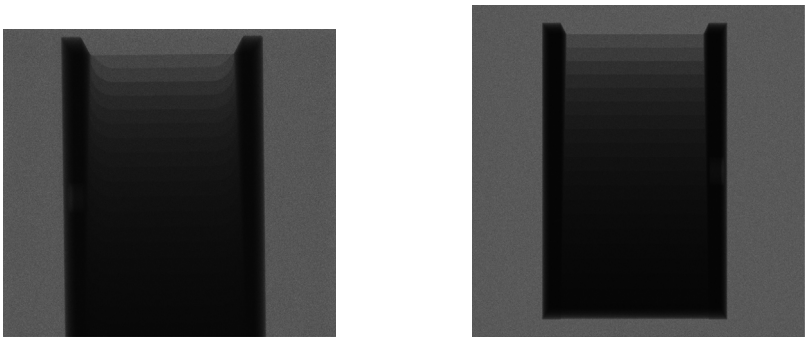

(a) Experimental. (b) Simulated.

Fig. 8. Variance of the pixel values computed from images used in Fig. 7.

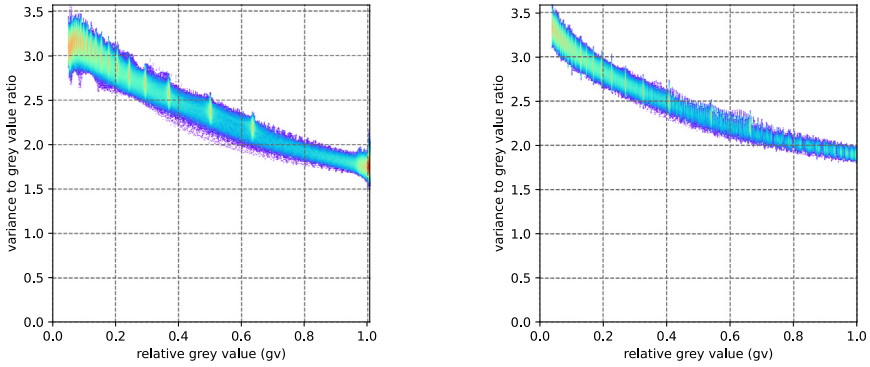

(a) Experimental. (b) Simulated.

Fig. 9. Plots showing the relationship between average pixel values (Fig. 7) and the variance due to the shot noise (Fig. 8).

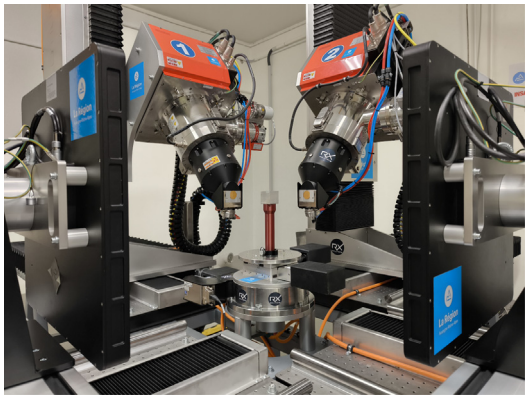

Fig. 10. Dual-beam high-energy XCT setup of the MateIS laboratory.

Table 1
CT scan parameters used during both the experimental scan and the digital twin.

Tube voltage	160 kV
Exposure	0.167 s
Current	200 µA
Beam filtration	0.4 mm of copper
Number of projections over 360°	1120
Detector pixel pitch [in mm]	0.150×0.150
Image resolution [in pixels]	1432 × 872
Source-to-object distance (SOD)	306.414 mm
Source-to-detector distance (SDD)	807.248 mm
Reconstruction algorithm	FDK
Voxel size [in mm]	$0.057 \times 0.057 \times 0.057$

5.2. Laboratory computed tomography: dual-beam XCT at MateIS

We are developing digital twins of specific beamlines, including selected labCT devices and a synchrotron. One of them is a new dual-beam X-ray computed tomography (CT) laboratory equipment of the MateIS laboratory (Lyon, France) [33]. The original concept of this design is that two beamlines are perfect twins, high energy (300 kV), oriented at $\pi/2$ to each other, and share the same rotation stage (see Fig. 10).

This dual-beam setup makes it possible to analyse a sample simultaneously from two different viewing angles. The noise model is under validation and a specific dual-beam calibration protocol has been proposed [34]. We report here the acquisition and simulation of an aluminium component of a tensile machine for in situ stress in scanning electron microscopes (SEM) because a CAD model is available. The most significant data acquisition parameters used during the experiment were inputed in gVXR. They are indicated in Table 1 for the dual-beam XCT device. All the parameters available in Table 1 are used as parameters of the simulation. Simulated X-ray projections of the CAD model are registered onto the experimental one (see Fig. 44). An optimisation algorithm moves the CAD model in the 3D space until the simulated and experimental images match. Fig. 11 shows a great level of similarity between images acquired with the actual device and its digital twin. In an ideal scenario, CT slices of a sample made of a single and homogeneous material correspond to binary images, i.e. air and sample. However, beamhardening, focal spot, impulse response of the detector and noise should corrupt to some extend the experimental data. All the artifacts visible in slices reconstructed from experimental data are also visible in the simulated ones (see Fig. 12).

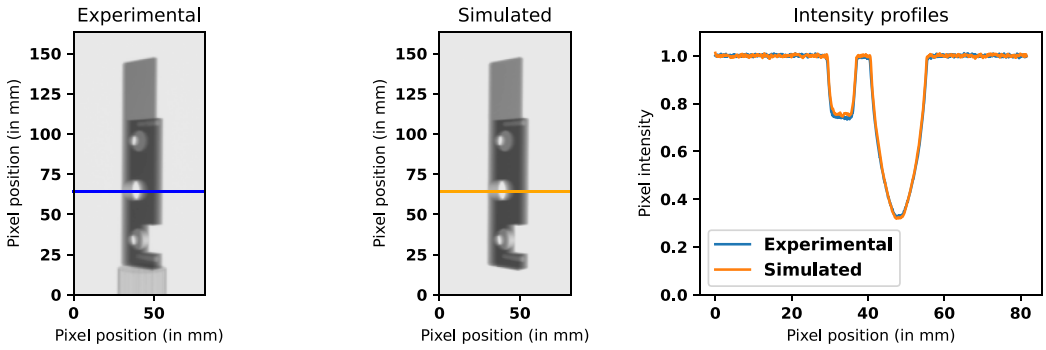

Fig. 11. Comparison between X-ray projections taken with a real dual-beam XCT laboratory device and its digital twin. For fair comparison, both projections are displayed using the same lookup table.

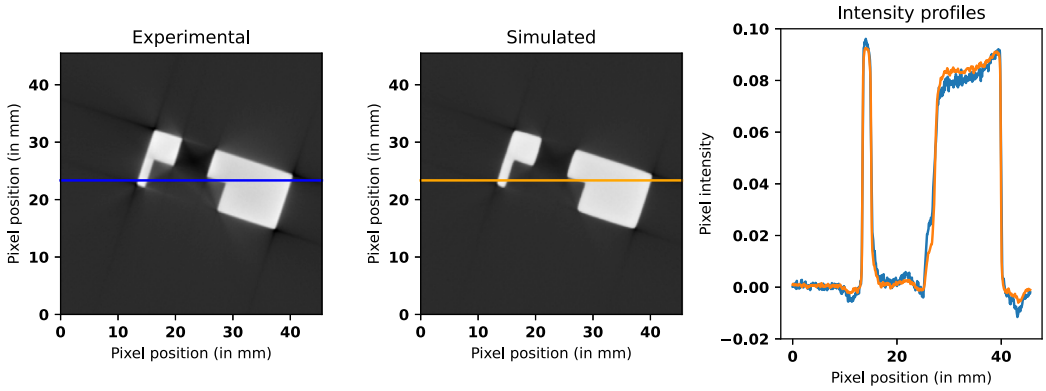

Fig. 12. Comparison between CT slices reconstructed from data taken with a real dual-beam XCT laboratory device and its digital twin. For fair comparison, both slices are displayed using the same lookup table.

5.3. Synchrotron CT: Dual Imaging And Diffraction beamline at Diamond Light Source

We are also building a predictive tool for synchrotron μ-CT at the Dual Imaging And Diffraction (DIAD) beamline of Diamond Light Source (DLS) [35] and integrating it in gVXR. DIAD is a dual-beam X-ray instrument for quasi-simultaneous imaging and diffraction, which operates two independent beams at energies of 7–38 keV (Fig. 13). Such digital twins will be integrated into gVXR and made available to any user in WebCT. The simulation model will be integrated into our web user interface for gVXR, WebCT (see Section 5.4). Beamline users will be able to (i) test specific CT scans from CAD models in realistic conditions, i.e. demonstrate the feasibility of their experiments before submitting a beamtime proposal, and (ii) optimise their scanning parameters before accessing the facility.

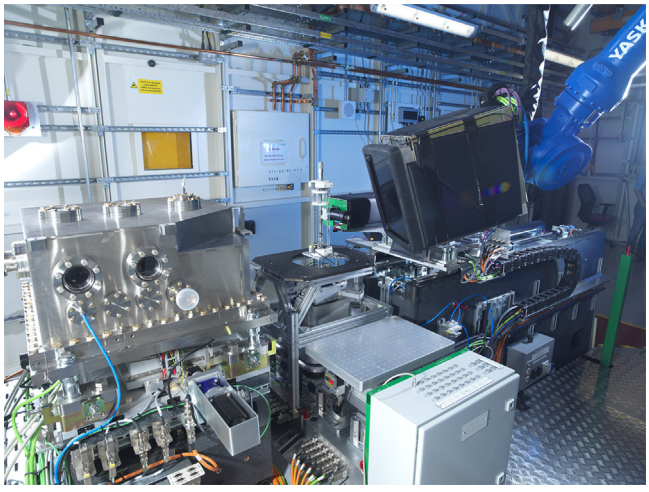

Fig. 13. A photograph of the DIAD beamline endstation, showing the KB optics on the left, and the imaging and diffraction detectors on the right.

5.4. Modern web-based simulation: WebCT

gVirtualXray's flexible API has allowed the development of WebCT (https://webct.io/, accessed: 4 Dec 2024) [36]. It is an interactive real-time web-based app for X-ray simulation, allowing anyone of any skill level to quickly simulate an X-ray scanner (see Fig. 14). The user can:

- Configure the X-ray spectrum and see the result in real-time, with support for different physical filters.
- Upload any 3D model and specify the corresponding material composition.
- Specify details about the detector, including pixel resolution, pixel pitch, scintillation,
- Change acquisition parameters (e.g. SDD and SOD, number of projections, etc.) and see the effect projections have on the reconstruction quality.
- Reconstruct the scans, and tweak for the best results.
- Save and export configurations, share source and detector parameters and load them into other applications.

As it is web-based GUI, no programming experience is needed. This is particularly suited for scan planning, answering feasibility questions, and teaching/training on X-ray systems without requiring access to expensive equipment.

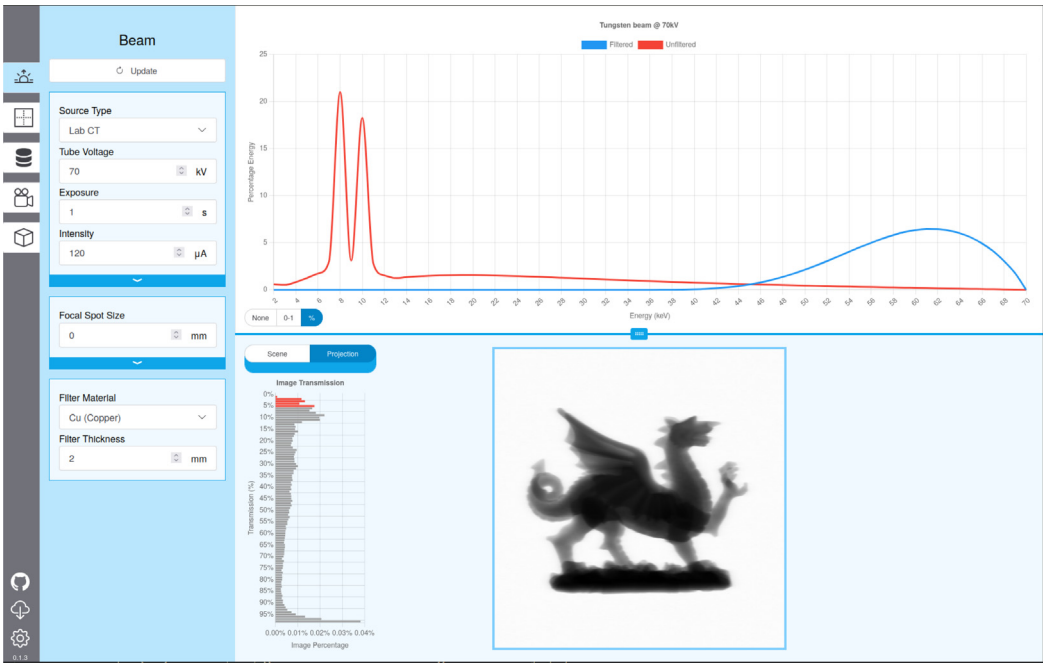

Fig. 14. Video 3 – Interface of WebCT in a web browser. A wide variety of X-ray settings allow quick, iterative scan planning and training. https://youtu.be/KZRkw_p0xbA.

Table 2
Description of the sample composition.

Material / Properties	Matrix	Kernels
Composition	ZrO_2	ZrB_2
Shape	Cylinder	Spheres
Diameter	8 to 10 mm	0.8 to 1 mm
Height	10 mm	N/A
Theoretical density	5.68 g/cm^3	6.08 g/cm^3
Measured density	3.23 g/cm^3	2.43 g/cm^3
Measured reduction of density	43%	60%

6. Enabling difficult experiments

6.1. CT scans of mock nuclear fuel

In NDT, XCT is commonly used to find defects in materials. Simulations were performed to ascertain the feasibility of CT scans of ceramic kernels held within a dissimilar ceramic matrix. Ceramic-ceramic matrix composites are garnering a great deal of interest in many applications, including as nuclear fuels for high-temperature gas reactors. The aim is to conduct experiments (i) to detect the interface between two very similar materials (in terms of composition and density), and (ii) to assess the defects in the structure that exist as a result of manufacturing methods in spherical zirconium diboride (ZrB_2) kernels held within a cylindrical zirconium dioxide (ZrO_2) matrix material.

A loss of density compared to theoretical values is expected due to the manufacturing process. Prior to the simulations, samples were produced. The diameter and height of the cylindrical matrix and the diameter of a typical spherical kernel were measured using a caliper. Their masses were assessed using a digital weighing scale. It makes it possible to compute the volume and material densities of the ZrB_2 kernels and the ZrO_2 matrix. This way, we can ensure the simulations are based on realistic values in terms of sizes, densities and material compositions. Table 2 provides a summary of the sample composition.

As the materials are close to each other and as the samples are relatively dense, i.e. opaque to X-rays, we will favour synchrotron radiation over the use of conventional X-ray tubes used in labCT. This is because synchrotron radiation can provide almost monochromatic spectra with high flux.

We use the Diamond Light Source, UK's national synchrotron radiation facilities, as an example. Two CT beamlines are available: the low-energy DIAD beamline, and higher-energy I12 beamline. A suitable energy must be selected (i) to maximise the contrast between the two materials, and (ii) to allow a sufficient level of radiation transmission through the sample. As CT images correspond to maps of linear attenuation coefficients, μ in Eq. (1), we aim at maximising the difference between the coefficients of ZrB_2 and ZrO_2. Fig. 15(a) demonstrates the linear attenuation coefficients of the matrix and kernels along the energies supported by both beamlines. The difference is the largest for 7 keV. However, when we apply the Beer–Lambert law in Eq. (1) using μ and **d** values corresponding to the sample, the transmission through the sample is 0%, i.e. hardly any photon reaches the detector behind the sample. The transmission remains low (below 5%) until roughly 95 keV (see Fig. 15(b)). At first sight, the issue is that we achieve the best absolute differences at low energies ($\mu_{ZrO_2} - \mu_{ZrB_2}$ in Table 3), but only high energies seem to be suitable to image the sample. Indeed, Table 3 also shows that the transmission remains below 5% until 110 keV. We must therefore ascertain that a difference in attenuation coefficient of 0.39, 0.28, or 0.22 cm^{-1} is significant enough to be visualised in reconstructed CT scans. The relative difference ($\frac{\mu_{ZrO_2} - \mu_{ZrB_2}}{\mu_{ZrO_2}}$) remains constant ($19.54\% \pm 1.11\%$) across all the energies, despite both material being close to each other. To select a suitable energy and make sure this relative difference in μ is sufficient enough, we performed simulated CT acquisitions at energies with the ranges [7, 38] and [53, 150] keV supported by the DIAD and I12 beamlines. Photonic noise and a few percent of harmonics were empirically added to the beam spectrum for added realism. Fig. 16 shows that according to our initial assumption energies below 85 keV were inappropriate. At 7, 38 and 53 keV, we were not able to scan the sample due to photon starvation. Fig. 17 shows CT slices reconstructed from experimental data acquired at the high energy beamline. As expected, no kernel is visible in the experimental images at 70 keV. Again, this is due to photon starvation as transmission is only 0.28%. As expected, 110 keV and 150 keV are suitable energies. However, 150 keV was selected as it can lead to faster scans due to a higher transmission rate.

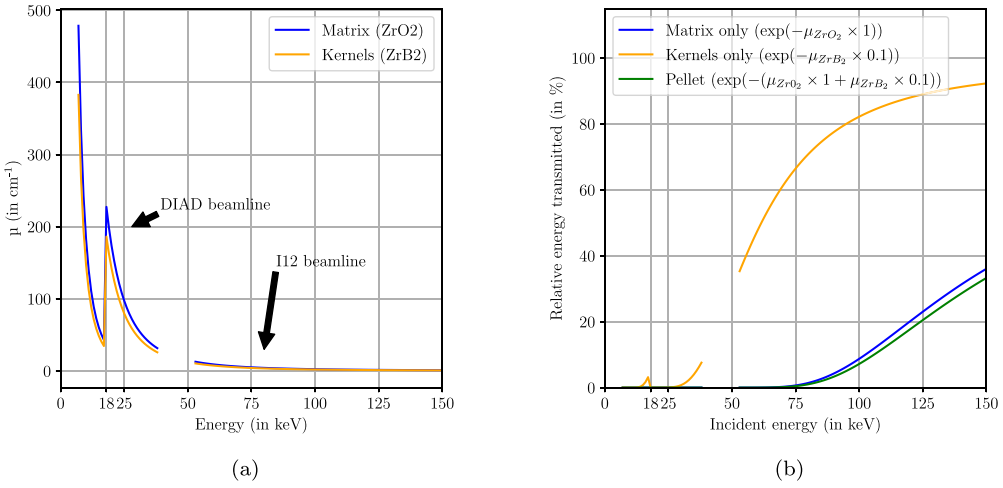

Fig. 15. (a) Linear attenuation coefficients and (b) relative transmission through the sample for the energy ranges at the low-energy DIAD beamline and higher-energy I12 beamline of the Diamond Light Source.

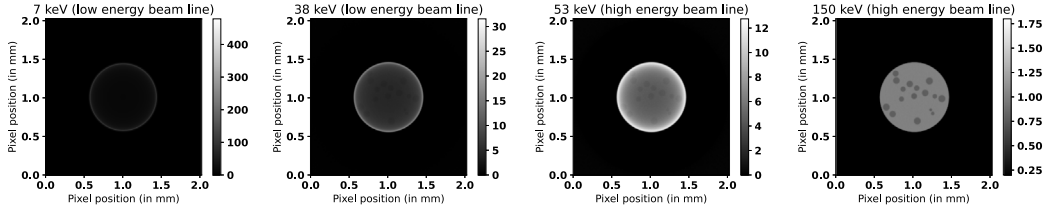

Fig. 16. CT slices of mock nuclear fuel reconstructed from simulated data.

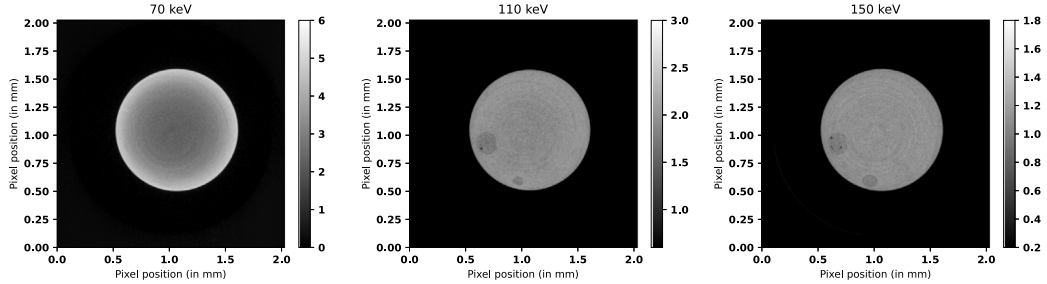

Fig. 17. Corresponding CT slices of mock nuclear fuel reconstructed from experimental data acquired at the high energy beamline. The same geometrical set up is used. The only change is the incident energy.

Table 3
Theoretical linear attenuation coefficients and photon transmission through the sample at energies supported by the CT beamlines at the Diamond Light Source.

Energy (in keV)	μ_{ZrO_2} (matrix) (in cm^{-1})	μ_{ZrB_2} (kernels) (in cm^{-1})	$\mu_{ZrO_2} - \mu_{ZrB_2}$	$\frac{\mu_{ZrO_2} - \mu_{ZrB_2}}{\mu_{ZrO_2}}$	Transmission
7	479.61	383.02	96.59	20.14%	0.00%
38	31.63	25.84	5.79	18.31%	0.00%
53	12.78	10.42	2.36	18.47%	0.00%
60	9.13	7.43	1.70	18.62%	0.01%
70	6.05	4.91	1.14	18.84%	0.28%
90	3.16	2.55	0.61	19.30%	4.61%
110	1.95	1.56	0.39	20.00%	14.96%
130	1.36	1.07	0.28	20.59%	26.79%
150	1.02	0.80	0.22	21.57%	37.05%

6.2. Sensor fusion and computer-generated densitometric images

Densitometric radiographic images is a technique that combines two radiographs that were produced with two different tube voltages. It is now possible to use ubiquitous motion sensing input devices originally developed for the video game industry, e.g. the Microsoft Kinect, to capture the 3D envelope of a real patient and save it as a 3D polygon mesh that can be used by gVXR. This 3D object can then be registered with radiographic images from that patient (see Fig. 18). The integration of this information (3D object + real radiographic images) has allowed for the acquisition of densitometric images, where one of the two images is acquired experimentally. gVXR proved to be very useful for generating the second image with another tube voltage [37]. This simulated image includes a simulated beam with new custom-defined parameters (kVp, mAs, hardening, filtration, etc.) but with the very same exact geometry, including that of the patient at the moment the radiograph was acquired.

Substituting one of the two images needed to generate a densitometric radiographic image leads to (i) a lower radiation dose for the patient than in traditional densitometric imaging, and (ii) a better image contrast than in typical single exposure radiographic imaging (see Fig. 19).

Also, to prepare for real sessions in hospital settings, gVXR was used to simulate the scenarios to be studied beforehand, prior to the application of any radiation [38].

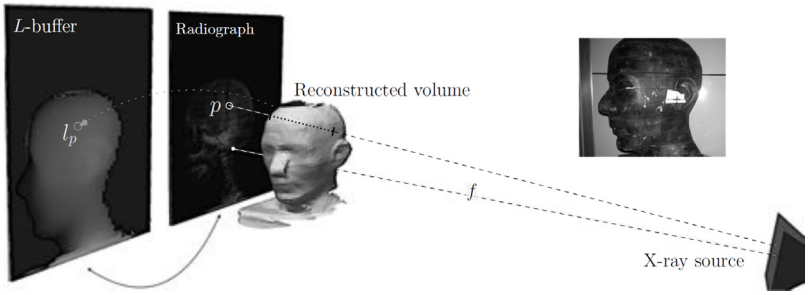

Fig. 18. Real path length (L-buffer) computed with gVXR of the contour data of a head-like anthropomorphic phantom.

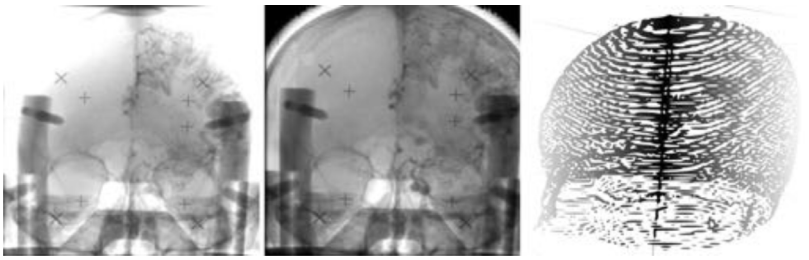

Fig. 19. Example of a densitometric image (middle image). The left radiograph represents the original X-ray instance and the rightmost image represents the traversed volume.

7. Quantitative evaluation of CT reconstruction algorithms

3D tomographic imaging serves as an essential complement to "conventional" 2D imaging for microscopic biological samples, as it provides direct insight into the probed structures while preserving their integrity. Among existing biological models, the *Caenorhabditis elegans* (*C. elegans*) nematode constitutes a well-characterised multicellular organism described in wide open-source databases, that encompass both anatomical and genomic information [39–41]. Its small size — approximately 1 mm in length — and reproducible internal structure makes it well suited for micro-imaging across multiple scales, spanning from tissular to cellular and even subcellular levels. Compared to other 3D imaging techniques such as confocal microscopy, X-ray emission induced by MeV-range protons or synchrotron X-rays provide access to the composition of the probed biological structures with unique capabilities: (i) multi-elemental chemical analysis; (ii) high sensitivity, down to a few $\mu g \cdot g^{-1}$. Such quantitative mapping can reveal dysfunctions in the homeostasis of chemical elements, which plays a pivotal role for example in the biological response to changes in the environment - due to factors like nutrition, stress, or exposure to exogenous compounds [42–45]. These imaging techniques involve scanning the sample with the penetrating radiation source (protons or X-rays) and measuring the transmitted radiations or the X-ray emission signal. For 3D imaging, the resulting projection data are then used to reconstruct the probed volume using advanced tomographic reconstruction techniques [46].

However, the acquired data may be incomplete, for various reasons: (i) temporal constraints, to limit the experiment's duration or to minimise radiation exposure; (ii) physical constraints, preventing access to certain measurement angles, constituting a "missing wedge". All these limitations are a source of errors in the reconstructed images, that need to be examined both on structural and quantitative aspects (accuracy of the calculated mass content). To our knowledge, no physical 3D sample standards exist, suitable to biological applications with low element concentrations. This prompted us to design a digital twin of *C. elegans*, and to develop a comprehensive data pipeline with the objective to validate quantitative tomographic reconstruction in the case of missing data [47,48]. The simulation pipeline begins with a CAD phantom of an adult hermaphrodite *C. elegans*, developed at LP2IB (Fig. 20), based on an anatomical model designed at CalTech [49–51]. The phantom's geometry is represented by a set of independent surface meshes compatible with 3D imaging simulation. For this purpose, the Python bindings of gVXR [8] were used to simulate at a first stage transmission tomography.

Subsequently, the developed mesh model is also used to generate a 3D voxelised version of the *C. elegans* phantom. In this context, a mass density distribution is assigned to the voxel data (depicted here with arbitrary constant values between 0 and 1) which serves as the ground truth. The developed data processing chain is illustrated in the following example (Figs. 21 and 22). Using gVXR, sinograms are simulated. Then, the reconstruction algorithm to be tested — *e.g.*, here, the Simultaneous Iterations Reconstruction Technique (SIRT) available in the ASTRA toolbox [52] — is applied. This approach enables direct comparison between the reconstructed volume and the reference voxelised phantom (Fig. 21).

To quantitatively assess the accuracy of the reconstruction, two metrics were computed: root mean squared error (MSE) and SSIM between the ground truth and reconstructed density images. Both metrics were calculated for the considered slice without any prior filtering. The SIRT algorithm utilised a minimal constraint of positivity, based on the assumption that the mass densities being reconstructed are positive.

A low value of RMSE was obtained (0.04) which indicates a relatively small average difference between the ground truth and reconstructed densities. For the SSIM calculation, a window size of 11×11 pixels was used, resulting in an SSIM value of 0.94. This high value suggests strong structural similarity between the two volumes, where 1 represents perfect similarity. Our main objective is to ensure an accurate reconstruction of the densities of each organ, as reflected by this high SSIM value. A complementary local comparison is conducted through image profiles (Fig. 22), which visually indicate the effectiveness of the reconstruction process in preserving the distinct density regions corresponding to different organs or structures.

This study demonstrates the successful application of gVXR in simulating tomography for assessing the accuracy of *C. elegans* imaging. This work marks an initial step towards further investigations focused on developing advanced methods to improve the accuracy and robustness of reconstructions, particularly in addressing cases of incomplete data.

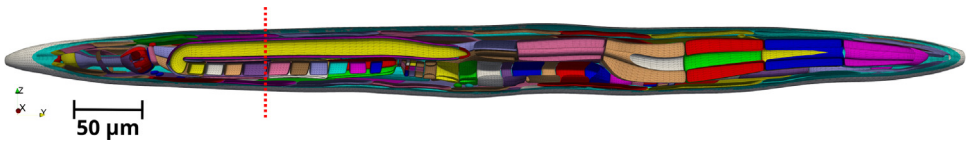

Fig. 20. A view of the 3D anatomy model of *C. elegans*. It is defined as a collection of independent triangular surface meshes labelled with different colours for a better visualisation. The vertical dashed line represents the slice used for the reconstruction in Fig. 21.

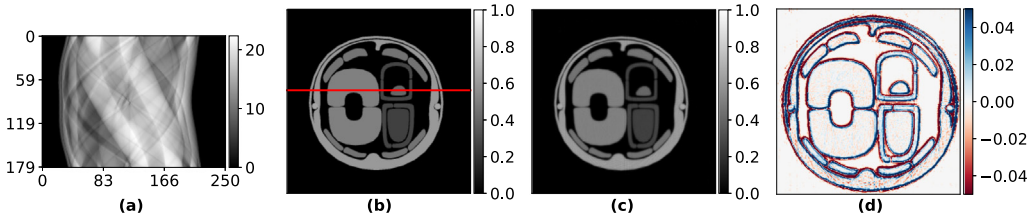

Fig. 21. Reconstruction of a slice of the *C. elegans* phantom. The sinogram **(a)** simulated with gVXR, here composed of 251 pixels (with a pixel size of 0.3 µm) and 180 projections with a 1°angular step, serves as input for the SIRT algorithm. This produces the reconstructed mass density distribution **(c)**, which is then compared to the voxelised image of the phantom **(b)**, here using the residual image **(d)** (a zoom is shown on the region of interest for a better clarity). The colour scale on the right of the images represents the projected mass density in 10^{-4} g cm^{-2} for **(a)** and the mass density in g cm^{-3} (arbitrary values) for **(b–d)**.

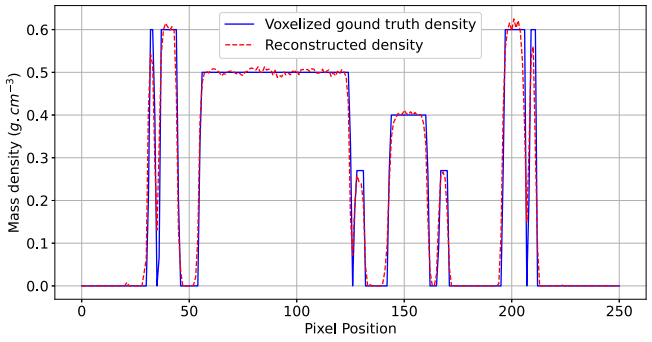

Fig. 22. Profile comparison of the ground truth and reconstructed density values. The profile is taken along the horizontal line indicated in Fig. 21-b.

8. Enhancing the simulation with motion

8.1. Drone-based radiography for wind turbine blades

Approximately 2%–3% of wind turbine blades require annual replacement, often due to defects in their internal composite layers [53]. These defects are invisible from the outside, prompting wind farm operators to use NDT techniques for internal inspections. A common method involves technicians rappelling down the blade while manually scanning each section with handheld ultrasonic equipment. However, this approach is costly, time-consuming, and potentially hazardous. Aerial radiography offers an autonomous alternative by using two drones equipped with the source and detector of a digital radiograph (DR) system, as illustrated in Fig. 23(a) [54]. Despite its advantages, this approach faces challenges from drone- and environment-induced disturbances, leading to motion blur in the images.

Mitigating motion blur requires both effective controllers to stabilise the drones and deblurring algorithms to enhance image quality. By integrating gVXR with a drone simulation environment, we can generate X-ray images corresponding to various trajectories, models, and disturbances, effectively closing the control system's feedback loop on image quality. The post-processing methods are integrated directly into this simulation pipeline to develop a comprehensive solution. The ability of gVXR to rapidly generate large datasets enables the application of learning methods to both drone control as well as image post-processing. Our preliminary research has focused on validating the accuracy of gVXR for motion-blurred images using an experimental dataset obtained with a commercially available portable DR system. An example of these results is shown in Figs. 23(b) and 23(c).

8.2. Motion artefacts with respiration simulation

gVXR was employed to model ghost artefacts during CT reconstruction caused by motion during acquisition. This approach was applied specifically to motion induced by respiration [3]. To achieve this, a respiratory model was implemented based on prior research conducted for interventional radiology training purposes [5,55]. To simulate the physiological mechanisms enabling lung inflation, we modelled the primary respiratory muscles, including the intercostal muscles and the diaphragm. Thoracic expansion was represented using a kinematic model (depicted in red in Fig. 24(a)), while diaphragm contraction was simulated with a deformable model based on the Chainmail method [56] (shown in blue in Fig. 24(a)). The lungs were attached to the ribs and diaphragm, deforming in conjunction with them, while the liver underwent translation (also illustrated in blue in Fig. 24(a)). The computational framework is hybrid, with mesh deformations calculated on the CPU and X-ray simulation performed on the GPU. Fig. 24(b) illustrates a CT scan reconstructed without respiration motion, whereas Fig. 24(c) demonstrates the capability to reproduce ghost artefacts due to the respiration motions.

The simulation was validated using patient data, where the anatomical geometries were manually segmented. Simulation parameters were automatically determined through optimisation based on evolution strategies. For this, clinical CT scans captured at maximal inspiration and expiration states were employed for each patient.

9. Machine learning

9.1. Early applications

gVirtualXray is also being used to produce a high number of realistic simulated images to train machine learning algorithms, including deep neural networks, which would not have been possible a few years ago. Lovitt created 2D images to estimate the length statistics of aggregate fried potato products [57]. Haiderbhai et al. trained generative adversarial networks to generate X-ray radiographs from photographs of hands [58]. Andreozzi et al. used gVirtualXray to generate noise free X-ray radiographs. Noise is added as a postprocess to study real-time edge-aware denoising in fluoroscopic devices [59]. However, it seems that most recent efforts have been focusing on image segmentation for diagnostic purposes, whether to detect pathologies in clinical applications or defects in NDT.

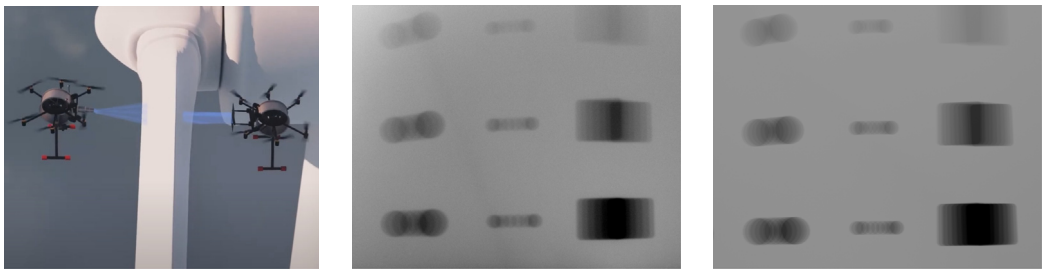

(a) (b) (c)

Fig. 23. (a) Dual drone NDT inspection system. (b) Image of a simple aluminium sample obtained with both the source and detector mounted on a motion platform. (c) Corresponding simulated projection from gVXR, aimed at replicating the blur structure. Note: The experimental image is contrast-enhanced for visualisation purposes.

(a) Model definition (b) No respiration motion (and then no artifact) (c) With respiration motion (and then with artifacts)

Fig. 24. Video 4 – CT scan artifact applied on the respiration application. https://youtu.be/fC1b1rGbtag.

9.2. Data augmentation for image segmentation

As an alternative to traditional computer vision methods, deep learning models have become increasingly common in image analysis, particularly for detection, classification, and segmentation tasks. However, these models require large amounts of training data to avoid overfitting and to promote model generalisation. In fields such as medical and material sciences, generating sufficiently large datasets poses significant challenges. For example, certain imaging techniques, such as tomographic scans in material science, can take hours to acquire. Additionally, annotating these datasets is time-consuming and may require several hours per slice for scans with particularly low contrast. Collecting these samples is therefore a major obstacle due to the time, cost, and human resources involved, as well as data anonymisation requirements [60]. To circumvent these constraints, various data augmentation strategies have been developed to generate synthetic images along with their corresponding labels. A common method involves the use of generative networks [61]. However, generative networks have limitations, including the need for large training datasets and often limited generalisation capabilities [62]. Another approach consists of combining gVirtualXRay with virtual models to produce large datasets of labelled synthetic images. These images replicate the noise and artifacts found in experimental data, accurately capturing real data variability while remaining representative and precise. For example, Phoulady et al. previously employed this method to automate defect detection in microelectronics [63]. We described below the latest applications of this approach for 2D radiographs, conventional X-ray CT, and spectral CT.

9.2.1. Lung nodule detection in 2D radiographs

The combined use of a virtual anthropomorphic model with gVirtualXRay allow the injection of artificial lesions, as well as the deformation of organ shapes and the modification of scanner settings to replicate the variability found in real datasets. We investigated whether training deep learning models on these large synthetic datasets could improve performance in pulmonary nodule detection.

Synthetic radiographs were generated using a thoracic model adapted from the virtual anthropomorphic model Z-Anatomy [64] (Fig. 25.a). Key anatomical structures — including skin, muscle, bones, blood vessels, and visceral organs such as the trachea, bronchi, lungs, and heart — were retained, and mesh simplifications were applied using Blender [65]. Material composition and density values were assigned to each tissue type in accordance with ICRP Publication 89 [66]. To simulate anatomical variability, tissue densities were randomly adjusted within a range of 0%–1%. Additionally, the dimensions of the entire model and each lung lobe were individually scaled along the x, y, or z axis within a 0%–4% range.

Pulmonary nodules were represented by a sphere of a diameter between 6 mm and 3 cm, randomly scaled in the x, y, or z axes. Between one and three nodules were randomly positioned within the lung structure and subjected to a random rotation (Fig. 25.b). Each nodule was randomly assigned a Hounsfield Unit (HU) value between −174 and 300.

To perform nodules detection, we used the state-of-the-art detection model YOLOv8m [67] with default optimisers and hyperparameters. Data augmentation included the default settings as well as a random rotation of 0–10 degrees. Training was conducted over 100 epochs. To evaluate models' performance, we used a standardised test dataset consisting of radiographs from the NODE21 database [68], which were not exposed to models during training (Fig. 25.c).

As a baseline for further comparisons, we first trained the model exclusively on real radiographic data (1767 images from NODE21 database), resulting in a sensitivity of 55.7%, a precision of 68.5%, and a F1 of 61.4% (Fig. 25.d). Training the model solely on synthetic data (8499 images) resulted in reduced performance, with sensitivity at 19%, precision at 8.8% and F1 at 12%, indicating limited effectiveness of synthetic data alone (Fig. 25.d). However, training the model on a combined dataset of real (1767 images) and synthetic radiographs at

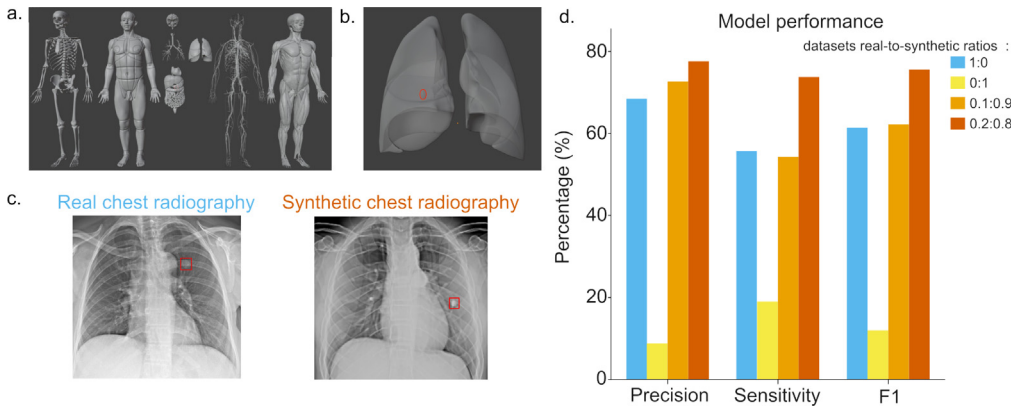

Fig. 25. a. Virtual anthropomorphic model (from Z-anatomy). From left to right : meshes represent bones, skin, visceral organs and brain, blood vessels, muscles b. Example of a synthetic lung model with an artificially inserted nodule (red) c. Example of a real chest radiography (left) from NODE21 dataset, and synthetic chest radiography (right). Nodules bounding box in red d. Model performance as a function of each training dataset.

real-to-synthetic ratios of 0.1:0.9 (i.e. 10% real radiographs and 90% of simulated radiographs) and 0.2:0.8 (i.e. 20% real radiographs and 80% of simulated radiographs) led to significant improvements. Precision increased to 72.7% and 77.6%, sensitivity to 54.3% and 73.8% and F1 to 62.2% and 75.6% respectively, representing an enhancement of up to 32% in sensitivity and 13% in precision over the baseline (Fig. 25.d).

These preliminary results demonstrate that model-based synthetic data shows promise for improving performance in deep learning models, highlighting its potential to enhance detection accuracy. This approach invites further investigation to assess its validity and versatility across other pathologies.

9.2.2. Simulation to real transfer of segmentation algorithm

X-ray tomography can be used for the generation of realistic representative volume elements for composite materials modelling. To translate the tomographic reconstruction into a geometry suitable for finite element simulations, the different phases need to be segmented and meshed. The segmentation problem can prove very challenging for low contrast scans where the phases have similar chemical compositions, such as carbon fibre-reinforced polymers. This is especially true in mesoscale scans of woven composites, where the yarns are impregnated with polymer matrix material reducing contrast further. Classical segmentation algorithms like thresholding and watershed often fail in separating the diffuse phase boundaries.

The applicability of gVirtualXray for synthetic training data generation in material science is demonstrated by training DeepLabV3 with a Resnet50 backbone using simulated tomograms [69]. The geometries to be scanned are generated with the open source software TexGen [70]. The segmented ground truths are received by voxelizing the input surface meshes in the same frame of reference as the simulated scan is performed. This is shown in Fig. 26. The model is trained on 30 synthetic tomograms, where the scan settings and geometry have been domain randomised. Inference on an experimentally derived (not-simulated) tomographic slice is shown in Fig. 27. This initial test shows promise, and it is likely a larger dataset and better tuned training procedure will yield better performance.

9.2.3. Spectral CT data simulation and material decomposition

The capacity of gVirtualXray to simulate spectral CT data plays a critical role in advancing material decomposition techniques within medical imaging. By generating synthetic data sets across high, low and conventional CT energy spectra, this technology supports the data required for the training process to build deep learning models. These models utilise pairs of reconstructed CT images and material density maps, created through the voxelisation of 3D meshes from segmented phantom STL files. This method reliably simulates the varied material properties and their distinct attenuation characteristics at different energies (see Fig. 28), which is crucial for precise material identification in spectral CT. The synthetic datasets closely replicate the variability and complexity of real clinical scenarios, enabling comprehensive training of algorithms without the significant costs and logistical challenges of gathering extensive clinical data. This approach not only enhances the precision and utility of AI models, but also demonstrates the flexibility of gVirtualXray in advancing the creation of sophisticated diagnostic tools through synthetic data generation.

9.3. Material characterisation

9.3.1. Defect detection and characterisation

In another material science application, gVirtualXray is used to automatically detect and characterise damages in composite and laminate materials by deploying it in data-driven predictor models [71]. It has been evaluated for different specimens under test, structure geometries, materials, and defects. They pose different coincidences between material (defect) and image features:

1. Homogeneous aluminium die casting plates with pore defects [72]
2. Composite fibre-metal laminate (FML) plates (aluminium and PREimPREGnated (PrePREG) layers with impact damages posing layer delaminations, deformation, cracks, and kissing bond defects (loss of adhesive contact between layers)).

Automated feature detection and marking in measuring images can occur on different levels:

- Region-of-Interest search;
- Feature marking and maps;
- Damage and defect classification;
- Damage and defect localisation;
- Global statistical aggregates (e.g. pore density, defect distribution).

One of the major issues in data-driven modelling in materials science is the low variance of data with respect to the parameter space. The number of features in measuring data is often limited. For example, impact damages, breakage defects, or tensile tests can only be applied once to a specimen. To overcome the limitation of the sparse experimental parameter space, simulation of measuring data (e.g. X-ray images) using parameterisable mechanical models should be used.

The entire workflow consists of different model and simulation levels:

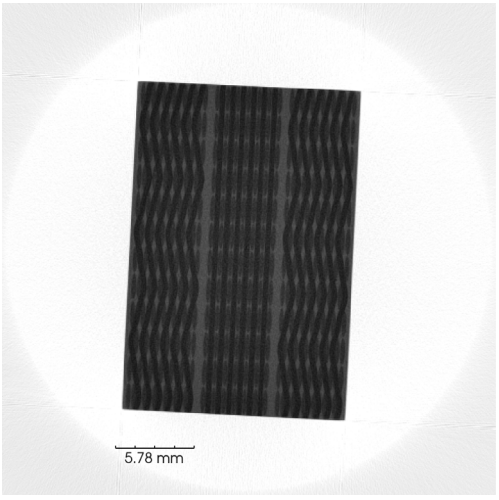

(a) A simulated tomographic slice.

(b) The slice in (a) segmented in to air, weft yarns, warp yarns, and pure matrix.

Fig. 26. A tomographic slice of a virtual recreation of a woven carbon fibre reinforced woven composite (a) is shown next to its corresponding voxelisation, i.e segmentation ground truth (b).

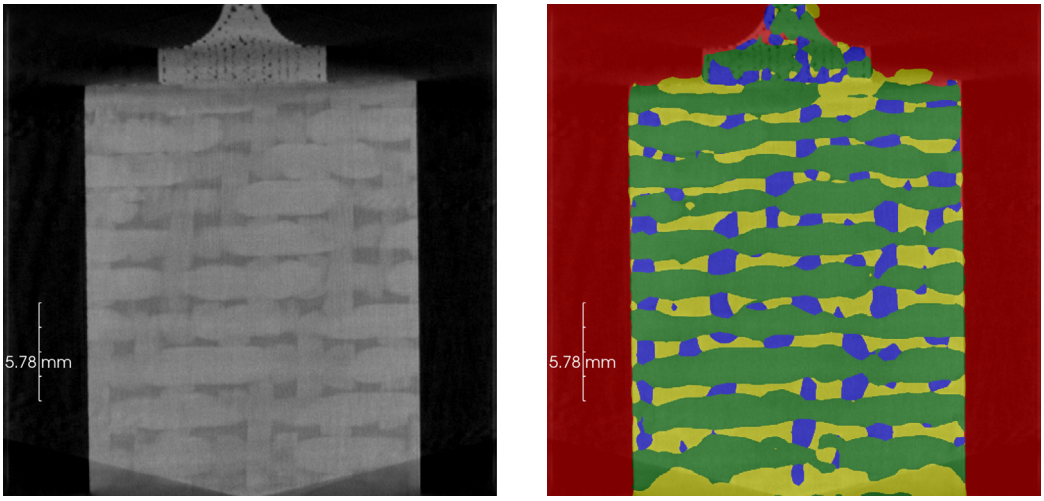

(a) A tomographic slice of a woven carbon fibre reinforced polymer sample.

(b) A machine learning derived segmentation. Air is shown in red, weft yarns in blue, warp yarns in green, and pure matrix is shown in yellow.

Fig. 27. A tomographic slice of a carbon fibre reinforced polymer woven composite (a) is shown together with a machine learning derived segmentation (b).

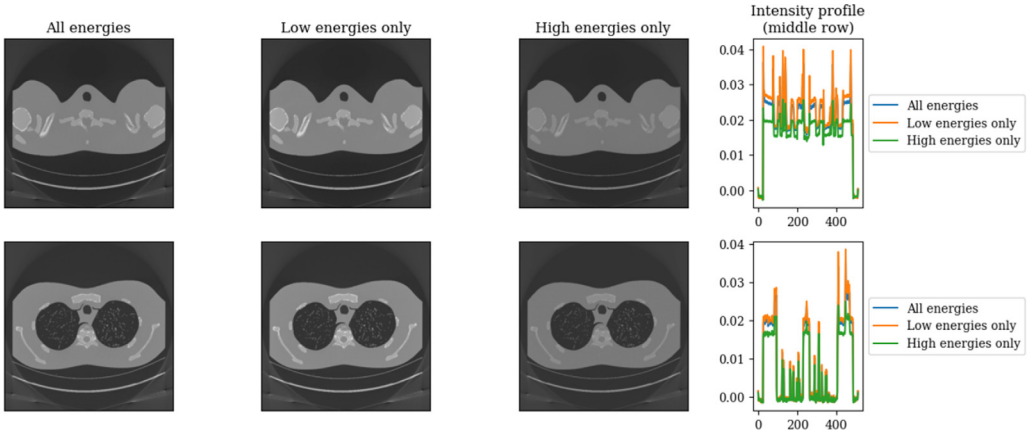

Fig. 28. Reconstructions of data simulated at different energy levels. Images are displayed using the same colour scale. Profiles are given in linear attenuation coefficients.

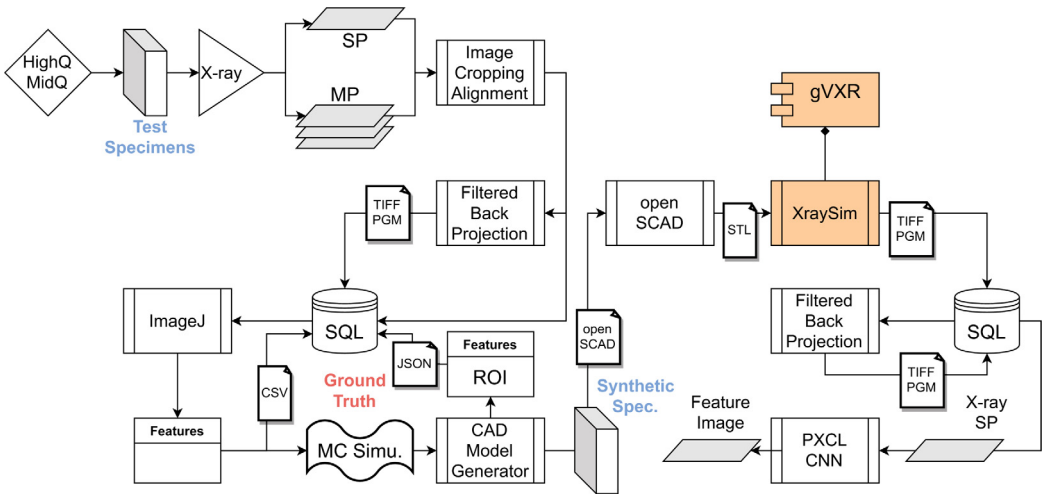

Fig. 29. Operational data flow.

1. Constructive Solid Geometry (CSG) modelling of material structures, defects, and damages ⇒ Parameterisable CAD model with ground-truth geometric feature tables (e.g. containing defect positions and sizes);
2. Transformation of the CSG model to a triangular mesh-grid model (STL format) using OpenSCAD;
3. X-ray image simulation (single- and multi-projection) using the gVXR library integrated in our XraySim tool [71] with a post-processing applying Gaussian and Binomial distributed noise to simulate noise from real X-ray image sensing systems;
4. In the case of radial multi-projection images, a filtered-back projection (FBP) algorithm is applied to reconstruct two-dimensional material slices;
5. Training of machine learning (ML) algorithms (e.g. convolutional neural network (CNN)-based pixel classifiers, SAM [73] or Detectron2 models [74]);
6. Test and validation;
7. Application of ML predictor models to real measuring data with experimental validation.

The CAD model is basically a digital twin of real materials and mechanical parts based on X-ray CT and optical micro-slice analysis, as shown in Fig. 29.

The mechanical model is used for the X-ray image simulation. The model consists of geometric objects with different material densities. CSG modelling is used to create complex 3-dim bodies. CSG consists of additive and subtractive Boolean operations combining shapes. A subtractive operation assumes a host material and a tool shape, e.g. using cylinders for creating holes. We are using the OpenSCAD tool [75] to create triangular mesh-grid models (STL format) that are processed by gVXR. Multi-material parts are imported with multiple STL files, each file is associated with a material density. All parts are merged internally with the respective material density. The pore analysis use-case is described in detail in [72]. The primary goal is automated pore annotation, detection, and characterisation in die-casted materials using X-ray radiography images. Due to the missing ground truth data (data annotation), the secondary goal is the training of the data-driven pore ML predictor with synthetic (simulated) data only. For this purpose, a parameterisable pore distribution model was designed based on CT analysis data. The basic CSG-CAD model for a plate with pores is shown in Fig. 30. Monte Carlo simulation is used to provide random distributions of locations, sizes, and orientations of pores. Pores will reduce the total material density along an X-ray path, resulting in brighter areas. The gVXR-based 'xraysim' tool was used to create X-ray radiography images (1024 × 1024 pixels), finally overlayed with Gaussian distributed random noise (average SNR=2 with respect to the pore intensity variation). Examples of noisy X-ray images and the output of the feature marking ML model are shown in Fig. 31. The feature marking predictor model (a classical low-complexity CNN model) could be trained with the synthetic images and applied successfully to real measuring images, producing pore feature maps with realistic accuracy (see Fig. 32). The false-negative and false-positive pixel marking error rates in synthetic X-ray images were below 1%. In contrast to the pore analysis use-case, impact damage analysis is still a challenge [76] and a work in progress. Impact damages in laminate structures create deformation and delamination, and at high impact energies, cracks occur, too. With respect to CSG modelling, the addition of defects is a subtractive operation, too, but must satisfy constraints, i.e. preserve the total mass-volume. A defect does not remove material, it shifts material, only, and considering non-compressible materials, the entire mass-volume does not change. An impact damage can be approximated with a Gaussian-like deformation.

A set of 800 radial projections was created using gVXR and finally reconstructed to cross-section slice images using a classical sine-wave filtered back-projection algorithm (using our *fbp* tool). The impact damage could be reconstructed with a high resolution, comparable to damages visible in real specimens and CT analysis, but showing small material inhomogeneities as a result of a material distribution violation in the CAD model. The synthetic data can be used to refine and validate the damage models as well as damage feature marking, classification, and characterisation algorithms.

The simulated X-ray images created by gVXR show high accuracy compared to real measured radiography and reconstructed CT images. The xraysim tool provides easy access to the underlying gVXR library, supporting CPU and GPU back-ends. Radial CT scans are performed automatically, reusing the imported geometric material model. We showed a complete modelling workflow, starting with a CSG model that can be easily generated and parametrised, then using OpenSCAD to create the material model with a triangular plane model processed by gVXR. Multi-material specimens must be provided separately by parts of the same material density. The different parts are merged in xraysim to one material model. Complex components and material combinations can be easily created. Even very complex models like fibreglass layers consisting of tens of thousands of fibres (approximated by cylinders) can be processed efficiently and accurately by gVXR. The computed X-ray image patterns correspond to real image observations. The synthetic data can be used to refine and validate the damage models as well as damage feature marking, classification, and characterisation algorithms.

```
rotate ([90,90,90])
difference () {
  rotate ([90,0,0]) cube([100,4,40],true);
  union () {
    translate([3.17,6.14,0.67])
      rotate ([0,0,-1.43])
      scale([1.15,1.12,0.31])
      sphere(r=0.5,$fn=20);
    translate([-16.66,-4.05,0.39])
       rotate ([0,0,40.14])
       scale([0.89,2.21,1.46])
       sphere(r=0.5,$fn=20);
...
  }
}
```

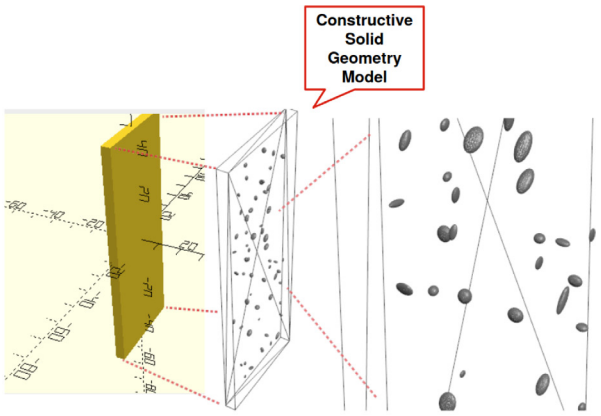

Fig. 30. CSG-CAD model of a plate with pores.

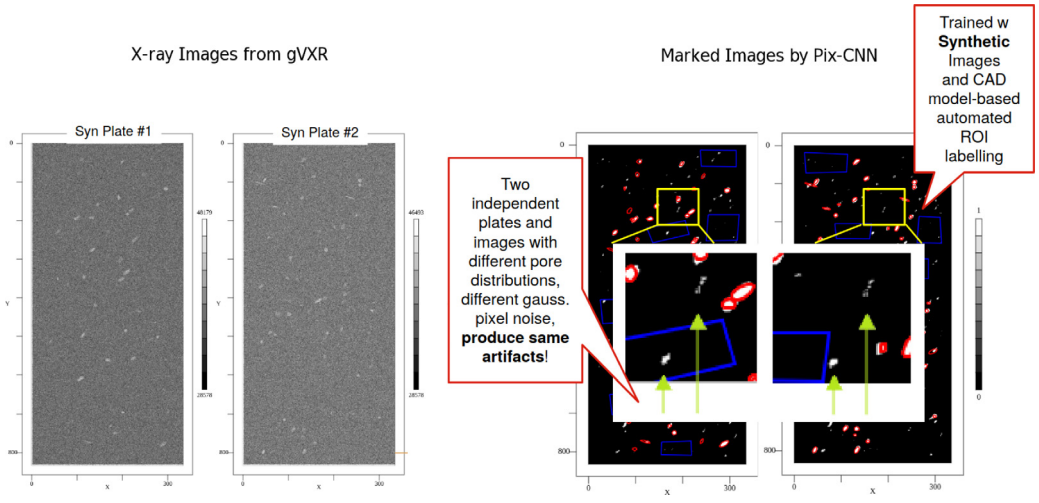

Fig. 31. False-positive markings of pores located at the same positions in different synthetic X-ray images with different specimens.

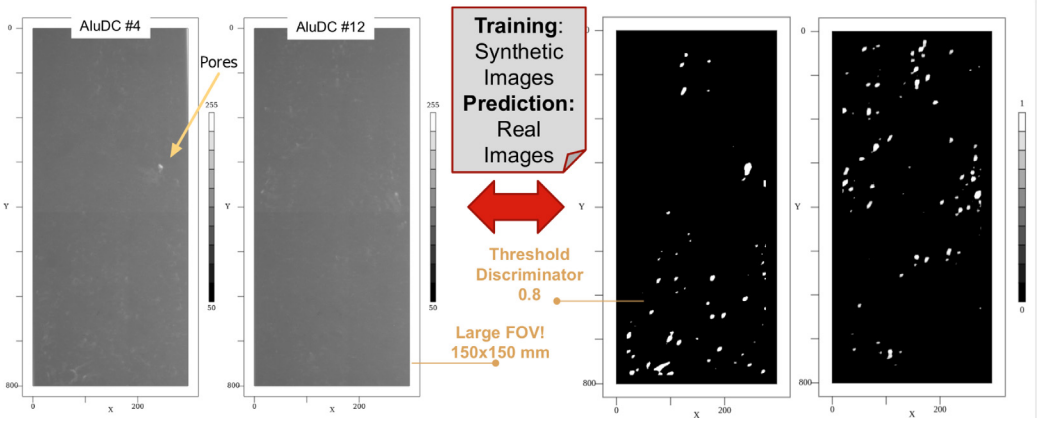

Fig. 32. Pore detection on real images using the ML model trained on synthetic data.

9.3.2. Characterisation of surface roughness for additive manufacturing

Additive manufacturing (AM), also known as 3D printing, is currently seen as one of the most promising methods to fabricate components for a wide variety of industries, including the aerospace, automotive and medical fields. As additive manufacturing techniques are quickly growing and becoming industry benchmarks, it is important to have rapid and easily applicable quality control and inspection techniques.

One of the main issues posed by surfaces in 3D-printed objects is the presence of defects and roughness. XCT is currently the only valid

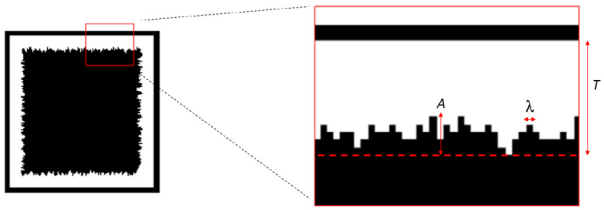

(a) On the left, a "slice" of the cuboid can be seen. In the middle, a zoomed-in section of the surface is shown, with the A being the amplitude, I the wavelength and T the thickness. The dashed red line is the baseline from which the rough surface was constructed.

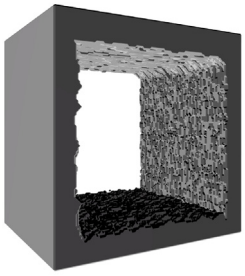

(b) Three-dimensional representation of one of the cuboids.

Fig. 33. Synthetic data created by the software.

method that can determine complete internal and external geometry without constraints of traditional tactile and optical techniques. However, XCT is a more expensive metrology tool and usually takes a longer time for part scanning and data processing, e.g. surface determination (identification of the material boundary of the scanned part), which limits its usefulness for industrial applications.

The study reported in this section investigates the use of deep learning (DL) as a tool to quickly determine where the "real" surface is in a reconstructed XCT image with a good level of precision. The aim is to improve the resolution of CT scans. To do so, synthetic virtual rough surfaces were created to obtain the "ground truth" data (Fig. 33(a)) using a newly developed plugin written in ImageJ macro language. The macro allows the generation of a cuboid hollow shape presenting various surface roughness (Fig. 33(b)). These cuboids were successively virtually scanned using X-ray simulation code gVirtualXray. Using simulations to generate virtual scans and data provided several advantages over real experimental scans: a full CT scan can take several hours to complete, whereas simulations are a time-efficient tool that can rapidly generate data for analysis. The trained neural network demonstrated significant success in improving the resolution of the rough surface images, as evidenced by a relative mean average error on the test data of 1.92% (Fig. 34). Furthermore, the deep learning output exhibited a 17-fold improvement in similarity to the true data compared to the input when measured by the mean square error. The main sources of error were found to be related to the lack of background noise inclusion in the scan simulations, and to the relatively small size and limited variety of the training data.

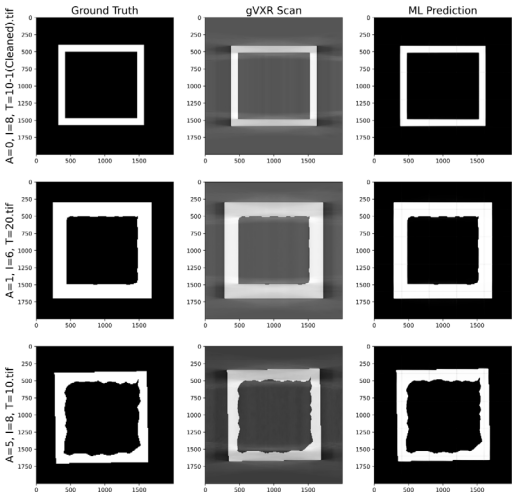

Fig. 34. Comparison of the ground truth, gVXR scan and neural network prediction for 3 different cube slices: the cube parameters are shown at the left of each ground truth image. The x and y axes are labelled with the pixel numbers.

10. Simulations to minimise or maximise an objective function

10.1. Hand pose estimation

Hand radiographs are commonly used to diagnose and stage diseases such as rheumatoid arthritis (RA) and other musculoskeletal diseases. RA is an autoimmune disease that predominantly affects synovial tissues and joints, although extra-articular features may be present, such as pathologies in the pulmonary and cardiovascular systems. Synovial joint damage, especially in the hands, can lead to limited range of motion and compromised dexterity. Determining the precise extent of damage is typically done with volumetric imaging such as CT or magnetic resonance imaging (MRI), depending on the stage and scope of the investigation. Since low socioeconomic status [77] is a risk factor, the cost of volumetric imaging often lends radiography as the only viable imaging modality.

Radiography is a projectional imaging technique, hence hand pose information is lost. 3D models of hands, both real and virtual, are a useful visual aid for patient-clinician interactions when diagnosis is initially made. This serves two important goals: (1) helping patients understand their disease and (2) facilitating shared-decision making when multiple treatments are available with similar risk/benefit profiles and when patient preferences are considered for treatment selection. Constructing a personalised virtual 3D model based on a patient's own radiograph makes the decision process visceral and more effective [78].

gVXR was used to register a generic 3D model of the human hand onto 2D radiographs from the MURA dataset (see Fig. 35(a) for an example) [79,80]. The registration was formulated as an optimisation problem. It was solved using the covariance matrix adaptation evolution strategy (CMA-ES) optimisation algorithm and allowed the recovery of hand pose. The objective function used was an average pixel-wise similarity between the real and simulated radiographs; only bones were considered.

Due to the projective geometries involved, there is a scale ambiguity, hence hand position in the simulated radiograph was used to match the scale of the hand in the real radiograph. The scale of each bone in the 3D model were variables in the optimisation problem and as a result individually scaled to account for individual anatomical features.

The problem is non-trivial because the hand joints have complex constrained motions with varying degrees of freedom. In spite of the complex constraints. Fig. 35(c) shows that the bone lengths and joint locations (i.e. angles) were recovered properly.

10.2. Feature size extraction in the case of strong imaging artifacts

Strong imaging artifacts in synchrotron-radiation micro-tomography may prevent the use of segmentation techniques to extract the size of structures in the corresponding images. For example, dark streaks and phase contrast fringes are clearly visible in Fig. 36(a) in a typical slice

(a) 2D radiograph. (b) Simulated image. (c) Error map.

Fig. 35. Example of registration of a generic 3D hand model on a 2D X-ray radiograph.

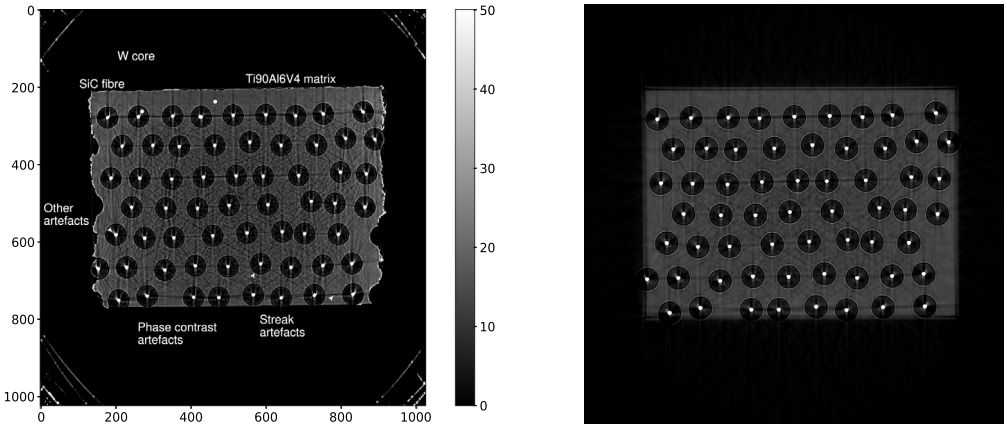

(a) Reconstructed from experimental data. (b) Reconstructed from simulated data.

Fig. 36. Synchrotron-radiation micro-tomography slices of a tungsten fibre-reinforced composite.

of a tungsten fibre-reinforced composite. It is possible to numerically model the real experiment with gVXR and optimise in objective functions the generation of simulated CT images, including their defects, leading to realistic artifacts [7]. The whole imaging chain was taken into account in the objective functions, including beam hardening, impulse response of the detector, phase contrast, and photon noise. Again, CMA-ES was used to solve the optimisation problems. The final image exhibit the same properties as the experimental image (see Fig. 36(b)) in terms of feature sizes and artifacts. It made it possible to automatically create of CAD models by image registration of X-ray projections, despite all the artifacts present in the experimental data. In a validation study, volunteers with experience in XCT and image analysis were asked to extract the size of the various features in Fig. 36(a). The tungsten cores proved to be difficult to analyse manually. Their diameter was biased by +28% (19.44 ± 1.45 μm) with respect to the nominal value recovered from a microscopic image (15 μm). It was not the case of the automatic analysis. The virtual experiment optimised to replicate the actual data led to tungsten cores of 15.80 ± 0.12 μm in diameter.

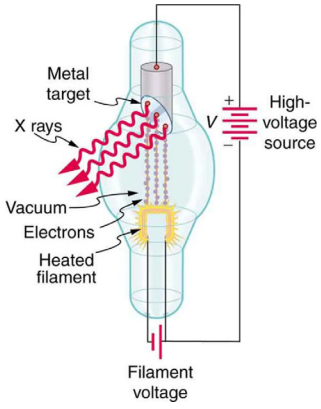

Fig. 37. Schematic representation of an X-ray tube. The electrons generated by thermionic emission at the cathode (filament) are accelerated by the applied voltage between the cathode and the anode (metal target). When the electron reach the anode, X-rays are generated.
Source: Reproduced from https://commons.wikimedia.org/wiki/File:OpenStax_CPhysics2e_29.11_X-ray_tube_sketch.webp.

10.3. Focal spot assessment

In the industry of non-destructive testing, common X-ray generating devices consist of a wire-cathode emitting an electron beam which is accelerated towards an anode (Fig. 37). The scattering of electrons on the anode causes the emission of X-rays via the Bremsstrahlung, Auger and X-ray fluorescence effects [81]. This type of device can be relatively compact and is therefore well-suited for industrial applications. However, this type of device suffers from some image blurring as the

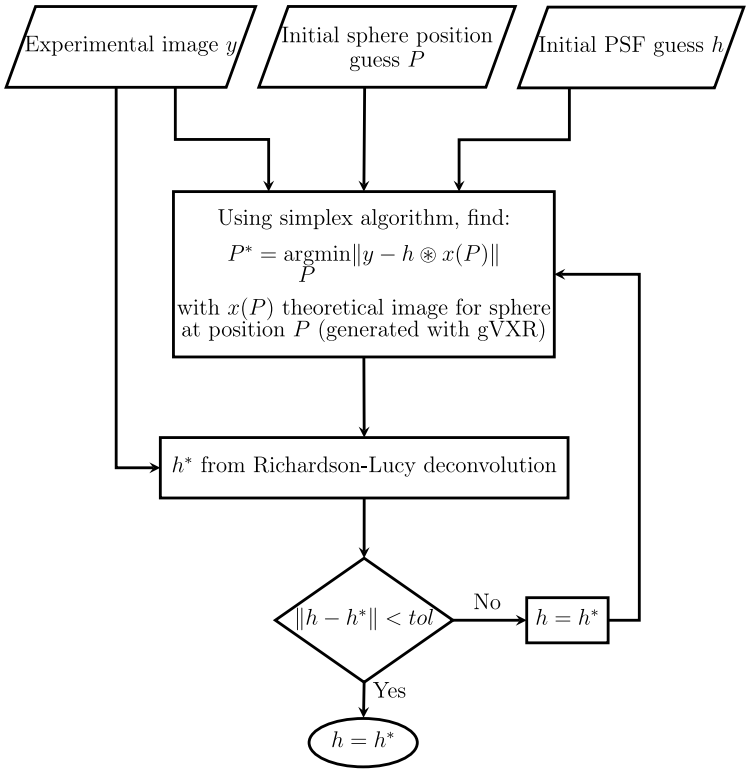

Fig. 38. Flow chart of the process for estimating the focal spot h from the X-ray image of a sphere. See text for details.

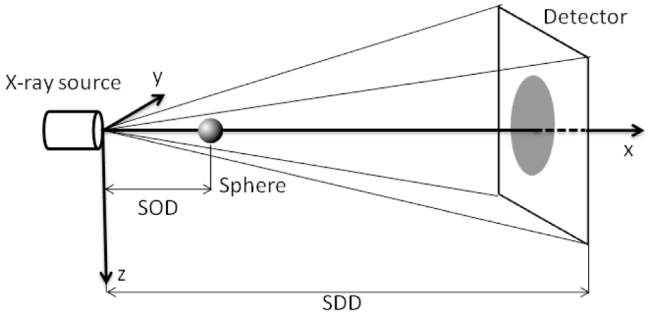

Fig. 39. Schematic of the experimental set-up for acquiring the X-ray image of a tungsten sphere.

electron beam impacts the anode on a non-punctual area; creating a focal spot. Controlling the size and shape of the focal spot is an important challenge as nowadays non-destructive testing and dimensional measurements require spatial resolution in the micrometer range [82–84]. Achieving spatial resolution of the order of the micrometer requires small focal spot sizes and large magnification factors, resulting in low X-ray flux; thus impeding the ability to scan thick mechanical pieces in a reasonable time frame. The X-ray flux may be increased by increasing the applied current, but usually at the expense of a larger focal spot size, and a consecutive loss in spatial resolution [81].

In this context, deconvolution techniques are a promising and full software solution for retrieving sharp X-ray images from blurred ones. Indeed, new deconvolution techniques have been rapidly developing last decade [85,86] and offer the possibility to use devices with large focal spots, while generating images with sufficient resolution. However, deconvolution techniques require the knowledge of the shape of the focal spot, or PSF. Numerous techniques exist for determining the focal spot, or PSF of a CT device, such as pin-hole camera [87], line and edge profiles [88–90], spheres [91–95] and other phantoms [96–98]. The most direct technique consists in using a pin-hole camera from which a focal spot can be directly extracted [99]. However, manufacturing a pin-hole camera is technically challenging [87]. Some other techniques aim to estimate only line profiles of the PSF (or line spread-function (LSF)) using thin wires, narrow slits or sharp edges [88–90]. Yet, tilting angles should be selected with care for taking into account the finite resolution of digital imaging system [89,100]. A more general method considers a small circular aperture from which the focal spot shape is deduced from edge profiles in all directions using filtered back projection [101,102]. Additional techniques rely on more complex shapes, such as coded masks [96], converging line group patterns (Siemens star) [98], spheres [91–95], and other phantoms [97]. Here, we consider sphere phantoms that present two main advantages: first, they are relatively easy to manufacture with a given precise radius, second, due to their symmetry, they do not require a precise mechanical alignment with respect to the measurement direction.

We propose to estimate 2D focal spots of a CT device from 2D images of tungsten sphere phantoms. Given a 2D experimental image of a tungsten sphere, a sharp theoretical 2D X-ray image with a punctual focal spot is generated using gVXR. The corresponding focal spot h is then estimated from the two theoretical x and experimental y images using a Richardson–Lucy [103,104] algorithm along with a total variation (TV) regularisation [105], see Eq. (2).

$$h^{(k+1)} = \frac{h^{(k)}}{1 - \lambda\, div\left(\frac{\nabla h^{(k)}}{\|\nabla h^{(k)}\|}\right)} \cdot \left(x\left(-(u,v)\right) \circledast \frac{y(u,v)}{x(u,v) \circledast h^{(k)}}\right) \tag{2}$$

(u, v) designates pixel position, $x\left(-(u,v)\right)$ is the 180° rotated image, λ is a regularisation parameter, div stands for the divergence operator, ∇ is the gradient operator, $\circledast$ is the convolution operator, and multiplication and division are performed component-wise. As proposed by Engelhardt and Baumann [106], the idea is to retrieve the PSF by inversion of a convolution process, where the experimental image is regarded as the blurred version of the theoretical image. A robust optimisation procedure is performed using the simplex method [107] for taking into account the uncertainties on the position of the sphere with respect to the X-ray source. The optimisation procedure is depicted in Fig.

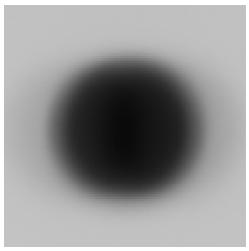

(a) 100 kV at 650 μA, 0.4 mm focal spot.

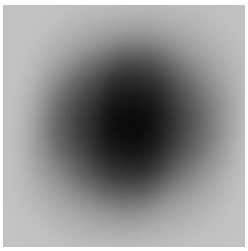

(b) 100 kV at 650 μA, 1.0 mm focal spot.

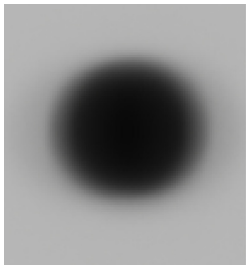

(c) 240 kV at 3333 μA, 0.4 mm focal spot.

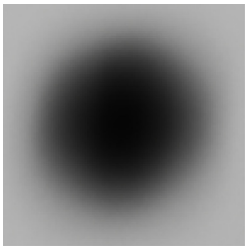

(d) 240 kV at 7500 μA, 1.0 mm focal spot.

Fig. 40. Acquired X-ray images of a 1 mm tungsten sphere at different voltages, currents and focal spots sizes using a *Comet MXR 320 HP 11 FB 90* tube. Note: for visualisation purposes, images were cropped and contrast enhanced.

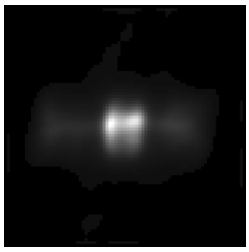

(a) 100 kV at 650 μA, 0.4 mm focal spot.

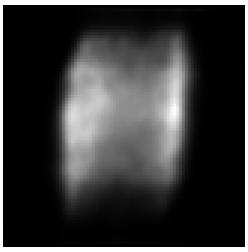

(b) 100 kV at 650 μA, 1.0 mm focal spot.

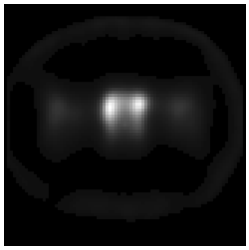

(c) 240 kV at 3333 μA, 0.4 mm focal spot.

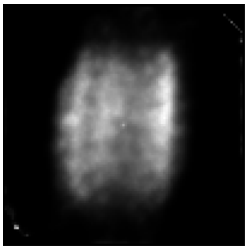

(d) 240 kV at 7500 μA, 1.0 mm focal spot.

Fig. 41. Corresponding 81 × 81 pixels focal spots estimated to the X-ray sphere images shown in Fig. 40.

38. gVXR plays a central role as it generates a new theoretical image $x(P)$ for each new guessed sphere's position P during this optimisation procedure. Especially, the fact that gVXR is fast in generating an X-ray image allows it to run the optimisation within a reasonable time frame.

Fig. 39 schematises the experimental set-up. Experimental images of a 1 mm tungsten sphere were acquired at different voltages and currents (see Fig. 40). The X-ray generator is a *Comet MXR 320 HP 11 FB 90* with two focal spots of 0.4 mm and 1.0 mm. The detector is a *Varex XRD 1620 xN CS* of 41 × 41 cm with 2048 × 2048 pixels and a pixel pitch of 200 μm. The SDD was 1150 mm, while the source to object (a.k.a. the sphere) distance was approximately measured at 90 mm.

Fig. 41 shows the corresponding estimated focal spots to the acquired X-ray sphere images of Fig. 40 using the algorithm described in Fig. 38. Fig. 42 displays the corresponding deblurred spheres of Fig. 40 using their related estimated focal spots of Fig. 41 through the "fast total variation deconvolution" algorithm [108]. Table 4 provides sharpness measurement [109] improvements before and after deblurring using the estimated focal spots. Finally, Fig. 43 shows profile comparisons between four acquired X-ray images displayed in Fig. 40, the theoretical images $x(P)$ generated with gVXR, and the theoretical images blurred with the corresponding estimated focal spots displayed in Fig. 41. From the profiles shown in Fig. 43 it can be seen that there is a good agreement between the experimental image of spheres and the theoretical images generated by gVXR blurred with their corresponding estimated focal spots.

10.4. Comparison of a manufactured object with its original CAD design

When a scanned object is manufactured from CAD, it is possible to register simulated projections of the CAD model onto the X-ray projections taken during a CT scan acquisition. An optimisation algorithm iteratively tweaks the position and orientation of the CAD model until the differences between the simulated and the experimental projections

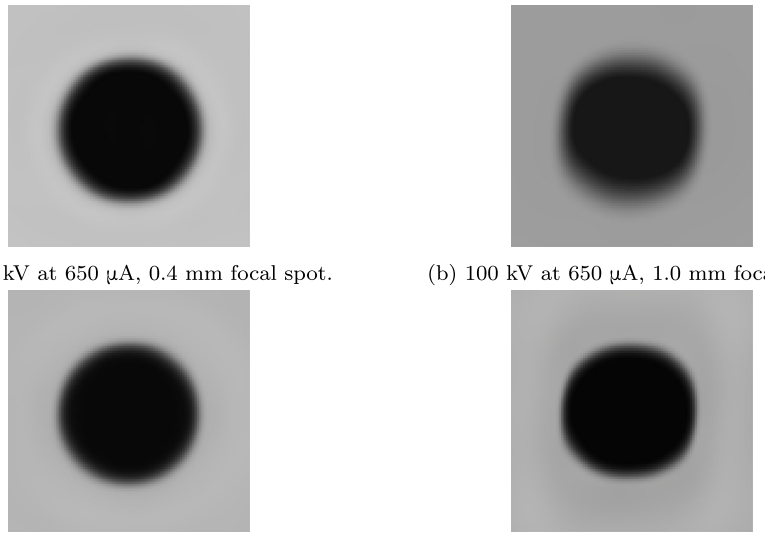

(a) 100 kV at 650 µA, 0.4 mm focal spot.

(b) 100 kV at 650 µA, 1.0 mm focal spot.

(c) 240 kV at 3333 µA, 0.4 mm focal spot.

(d) 240 kV at 7500 µA, 1.0 mm focal spot.

Fig. 42. Deblurred spheres of Fig. 40, using corresponding estimated focal spots of Fig. 41. Note: for visualisation purposes, images were cropped and contrast enhanced.

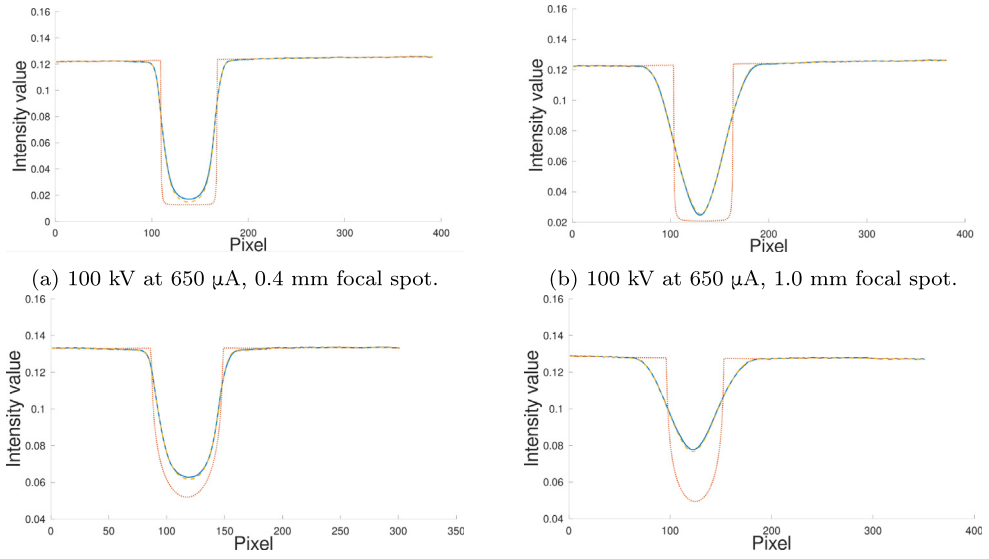

(a) 100 kV at 650 µA, 0.4 mm focal spot.

(b) 100 kV at 650 µA, 1.0 mm focal spot.

(c) 240 kV at 3333 µA, 0.4 mm focal spot.

(d) 240 kV at 7500 µA, 1.0 mm focal spot.

Fig. 43. Profile comparisons between four acquired X-ray images displayed in Fig. 40 (continuous blue line), the theoretical images $x(P)$ generated with gVXR (dotted red line), and the theoretical images blurred with the corresponding estimated focal spots displayed in Fig. 41 (dashed yellow line).

Table 4
Sharpness indices [109] of the X-ray images of a tungsten sphere before (Fig. 40) and after (Fig. 42) deblurring, using the estimated focal spots shown in Fig. 41.

Sphere image	Before	After	Improvement
100 kV, 650 µA, 0.4 mm	0.8916	5.5856	+4.6920
100 kV, 650 µA, 1.0 mm	0.2854	3.2678	+2.9824
240 kV, 3333 µA, 0.4 mm	0.8768	4.2807	+3.4040
240 kV, 7500 µA, 1.0 mm	0.2697	7.8034	+7.5337

are minimised. Fig. 44 illustrates the whole process. We show here the results on an optical component (mirror petal) for a nanosatellite (< 10 kg) produced with AM (see Fig. 45) [110], but the technique has been applied on other samples.

An internal lattice (triply periodic minimum surface diamond lattice) was used in the design (CAD) to reduce the mass by 44%. Finite element analysis and prototyping experiments were conducted to ascertain the robustness of the design to ensure optimal performance and manufacturability. The selected model was 3D printed using laser powder bed fusion in an aluminium alloy (AlSi10Mg) and postprocessed using conventional machining, followed by single point diamond turning to generate the reflective surface. XCT acquisitions were performed to assess the presence of porosity or fractures and the accuracy of the print versus the CAD. The SDD was 1179.29 mm and the SOD was 647.23 mm. The pixel pitch of the detector is 0.2 mm. The same scan was replicated virtually after 3D registration, i.e. same geometrical properties, material compositions, tube voltage (150 kV) and filtration (0.5 mm of copper). Fig. 47 shows that simulated projections of the CAD model are close to the experimental ones after the registration. The correlation between the experimental and simulated X-ray projections is above 99.50% and SSIM is 0.95. The differences are mostly due to the foam used to keep the sample in place during the scan, which

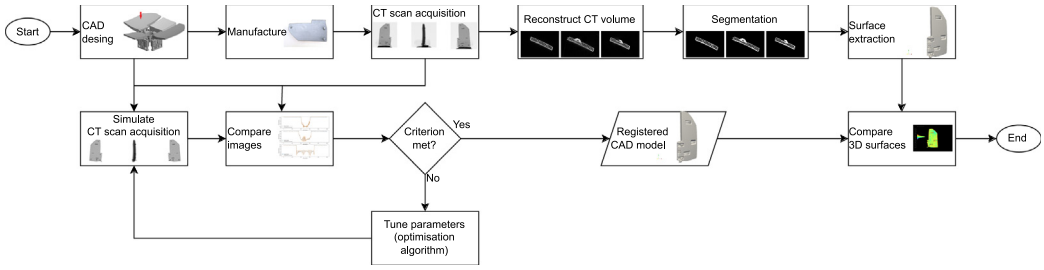

Fig. 44. Flowchart of the process to compare a manufactured object with its original CAD design.

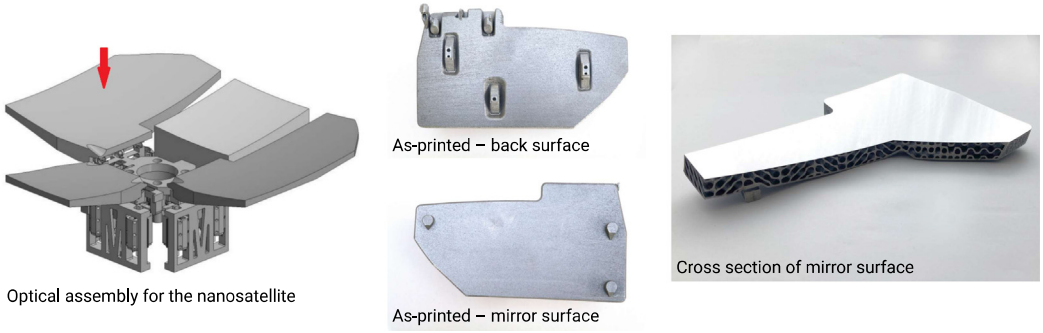

Fig. 45. (left) the nanosatellite optical assembly highlighting the mirror petal; (middle) the as-printed design that underwent XCT acquisition; and (right) a cross section through the reflective surface showing the internal lattice.

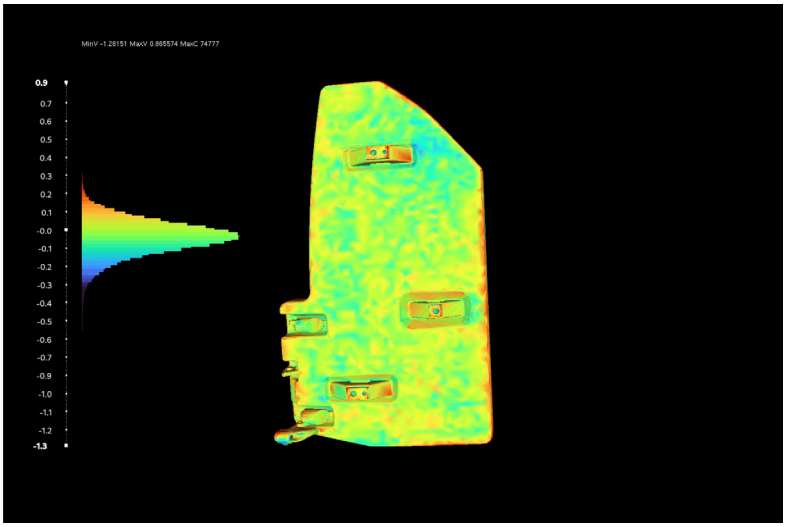

Fig. 46. Discrepancies [in mm] between the 3D surface models from the original CAD with the one extracted from the segmentation of the experimental scan.

was not modelled in the simulation. Intensity profiles (see Fig. 48) through the middle row of the corresponding images show that the simulated images are perfectly aligned with the experimental ones after the registration. Again, pixel intensities are slightly higher in the simulated images for pixels corresponding to the foam.

It is now possible to visually compare and quantify differences (e.g. using the Hausdorff distance) between the 3D surface models from the original CAD with the one extracted from the segmentation of the experimental scan (see Fig. 46). The colour used in the visualisation is related to the error, making it easy to identify where the sample is smaller or larger than the CAD model. Table 5 shows that the 3D printing errors are very small, 0.02 mm on average, which is well below the size of a voxel (0.22 mm).

Table 5
Displacement (error between manufactured and CAD).

Absolute value	mm	Pixels
Min	0.00	0.00
Max	1.27	5.76
Mean ± stddev	0.02 ± 0.06	0.11 ± 0.26
RMS	0.06	0.28

10.5. Assessment and optimisation of industrial XCT performance

It is well known that the performance of an XCT scan depends on many factors. Furthermore, the performance of an XCT scan is likely to vary across the reconstructed volume of a given component. For example, in NDT for industrial components using polychromatic

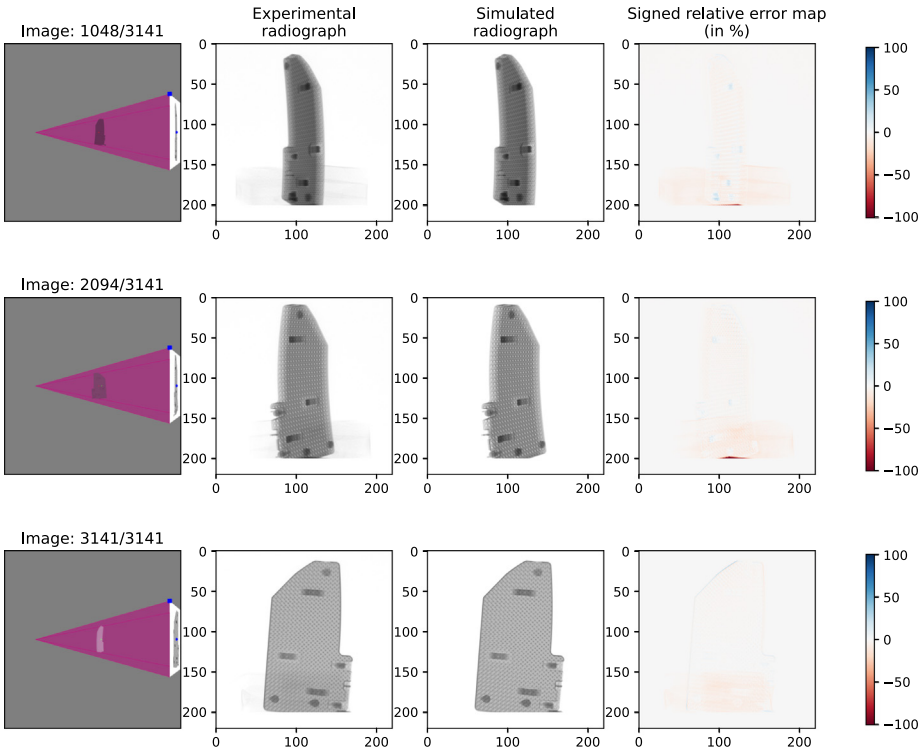

Fig. 47. Comparison between corresponding experimental and simulated X-ray projections after registration.

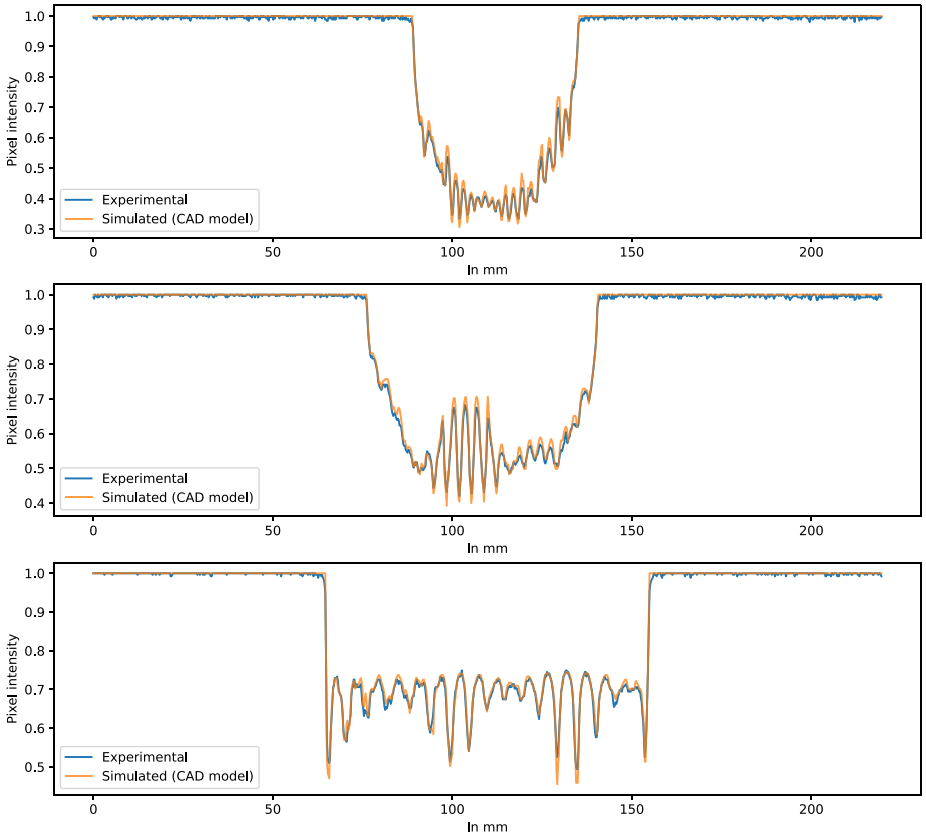

Fig. 48. Intensity profiles through the middle row of images presented in Fig. 47.

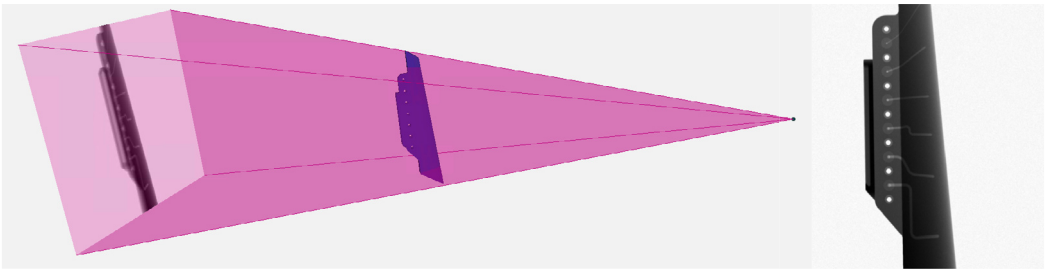

(a) The arrangement of the part with respect to the source and detector. (b) The initial projection. Note that the 3D visualisation is a built-in feature of gVXR. It can be used interactively.

Fig. 49. The initial simulation setup for the DRAMA aerofoil blade component, prior to optimisation.

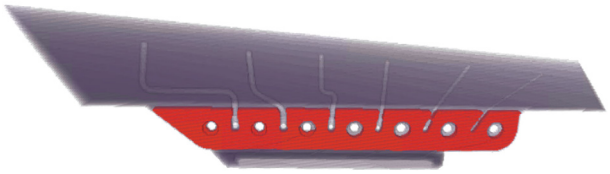

(a) The bracket region of interest is highlighted in red with respect to the aerofoil geometry.

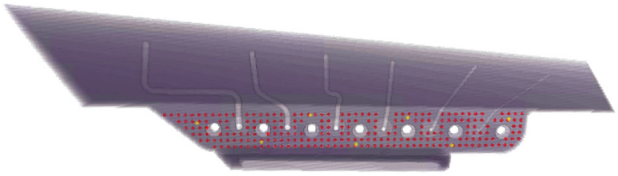

(b) Defect seed locations (not defects themselves) are highlighted. The locations highlighted in red were used in the inspection performance assessment, while the locations highlighted in yellow were used to compute the objective function during the optimisation.

Fig. 50. A voxelised representation of the geometry showing regions of interest used for the analysis and optimisation.

sources, the contrast generated by a defect in the part is expected to vary depending on the amount of material being penetrated across each projection in the scan.

While the performance will clearly be affected by modifying the X-ray source parameters and modifying the pose of the part, it is difficult to gain a good understanding of the spatial variability of the inspection performance for a given setup without running a significant experimental campaign utilising a large number of samples with defects deliberately seeded at specific locations. However, experimental testing can be unattractive, not only due to associated high cost and material waste, but it requires the development to be mature enough for component manufacturing. This is often not the case for newly developing products, and often the design may need to be re-iterated, and sometimes re-designed to alleviate any identified inspection challenges.

The MTC has developed a Python framework to automatically configure gVXR setups, seed defect geometries into a part, and track the positions and orientations of these defects in 3D space as the part is reoriented. From this, defect positions in each projection and the reconstructed volume are also computed, which will become important in the calculation of an objective function that aims to maximise the Inspection Performance Map [111] at defect locations.

Depending on the application, the user can seed defects in a stochastic manner, weighting defect locations to specific regions of the part, or with specific behaviours such as clustering or proximity to the component surface. Furthermore, the defect geometries used can be a specific defect definition (such as a pore of a specified diameter), or can be taken from a library of pre-saved defect geometry STLs extracted from genuine XCT datasets. The size and material of defects can be redefined as desired, and multiple defect types can easily be seeded into the same part. The intention of this framework covered two goals, firstly, to provide a method for quickly generating a large number of randomised defect indication images for training automated defect recognition algorithms (using randomised locations and defect definitions), and secondly, to provide a method for assessing the variability of defect detectability across the part to locate inspection blind spots (using predefined locations and a rigid definition of a defect). The work presented in this section focuses on the second application.

While the detector resolution has been defined to be 750 by 750 pixels, a super-sampling factor of 3 was used (resulting in a simulated resolution of 2250 by 2250 pixels), and then re-binned to the original resolution. Across several X-ray simulations we have used, we have found this super-sampling approach to be essential for eliminating aliasing artifacts around features that span only a few pixels at the original resolution.

The part geometry used was the Digital Reconfigurable Additive Manufacturing facilities for Aerospace (DRAMA) additively manufactured $250 \times 15 \times 70$ mm aerofoil in Ti-6Al-4V with laser powder bed fusion. The system being modelled was based on a Diondo D2 system, with a 225 kV source and a 400 mm by 400 mm detector, shown in Fig. 49. For computational speed, the detector resolution was set to 750×750 pixels, a quarter of the genuine system. The computational hardware was a workstation using an AMD Ryzen Threadripper 1950X (16 cores), NVIDIA Titan XP, 128 GB RAM (2800 MHz) and NVMe SSDs.

10.5.1. Calculating an inspection performance map

To assess the inspection performance before and after optimisation, this work sought to create an inspection performance map similar to that shown in previous work [111]. For generating predefined locations, a Boolean voxelised representation of the part geometry was derived using a voxelisation algorithm on the part STL with a voxel spacing of 0.4 mm. A region of interest voxel map was then defined by taking voxels which overlapped with the bracket attachment section, shown in Fig. 50(a). The region of interest was then used as a weighting array for the defect generation algorithm (weight = 1 inside this region, and 0 outside). In this case, the weighting volume was slightly offset from the surface of the part to avoid creating surface-breaking defects, as the performance metrics used here do not work well around the sharp edges of the part. From here, a grid sampling algorithm was used to take every 7th voxel and use these as hypothetical defect locations, corresponding to a sampling spacing of 2.8 mm. The result was a total of 234 hypothetical defect locations, shown in Fig. 50(b). The defect definition used was a spherical void of diameter 0.5 mm.

Each defect in the grid was assessed using the approach shown in Fig. 51. Each defect needs to be assessed individually, and rather than

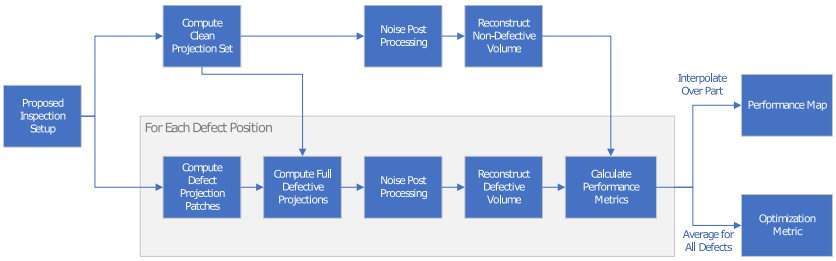

Fig. 51. Diagram showing the simulation workflow for generating defective data and calculating performance metrics.

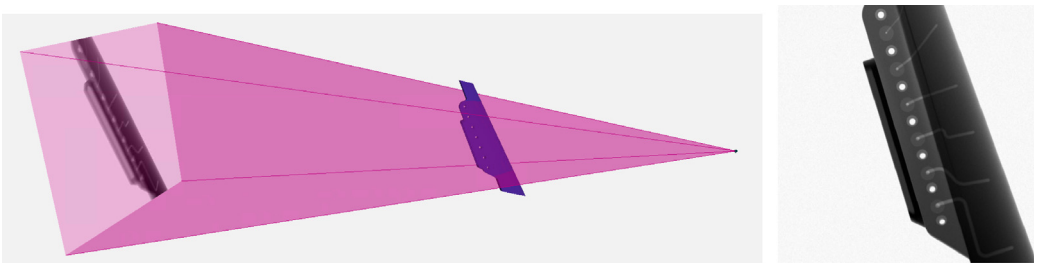

(a) The arrangement of the part with respect to the source and detector. (b) The initial projection.

Fig. 52. The initial simulation setup for the DRAMA aerofoil blade component, after optimisation.

calculating a full projection set for each defect, it was found to be more computationally efficient to compute a "clean" (non-defective, no noise), projection stack for a given setup, and then assess each defect by simulating small 11 × 11 pixel patches of the detector, with each patch centred on the defect location as the part rotates around the scan. Defective image patches were then stitched back into the clean projection set to produce a full projection image set containing the defect. An additional benefit of computing patches is that the computational impact of super-sampling is practically negligible when sampling such small patches of the detector. Once each defective projection stack was generated, the stacks undergo Poissonian noise post-processing and reconstruction operations using the ASTRA toolbox. When adding noise to the projections, unique noise images were pre-generated and reused for each projection. This approach ensured that the noise patterns remained consistent across each projection, except where the noise was scaled based on the intensity changes incurred by adding each defect. Finally, the results were interpolated across the region of interest to produce a final performance map that will be shown in the next section.

While there are several approaches for assessing image quality [112, 113], there are usually additional bespoke image processing steps required to implement these approaches. The metric used here was based on the contrast-to-noise ratio (CNR).

To calculate the contrast metric for each defect, reconstructed 30 × 30 × 30 voxel volumetric patches were compared with and without the defect. A difference volume was computed, and a 3D mask of the defect was extracted using a slight Gaussian blur (with a sigma value of 0.5 pixels) followed by Otsu binarisation thresholding, and a dilation operation. The difference values that overlap with the defect mask were extracted and averaged, thus giving a representation of the defect contrast.

To calculate the noise metric in the vicinity of each defect, the non-defective volumetric patch underwent edge-preserving bilateral filtering and was subtracted from the original to produce a volume that should only contain noise. This patch was then overlaid with the defect mask calculated earlier to extract voxel noise in the defect vicinity. Finally, the standard deviation of these values was taken to give a representation of the noise. By dividing the contrast metric by the noise metric, the final CNR metric can be deduced. As will be seen in the visualisations in the following section, the noise metric is quite susceptible to local variations, which we expect is related to the resolution of the sampling grid used in Fig. 50(b). Many different approaches were tested to reduce this variability, but the metric described was found to give the most consistent results.

To process all defects and complete the inspection performance map, the computation took 74 min in total, with 33 min spent calculating projection images, 30 min performing reconstructions, and the remaining time spent with additional processing of the data. This could be reduced by further optimisation of the implementation, but for the purposes of making a performance map, this computation time was acceptable.

10.5.2. Optimising the scanning geometry

The SciPy Nelder–Mead optimiser was used to optimise the geometrical parameters of the setup using the setup shown in Fig. 49 as a starting point. The six parameters addressed by the optimisation were: two parameters to set the orientation of the part (the rotation around the CT axis was ignored), three translational offset parameters to position the part with respect to the CT axis, and finally, the source-to-object distance (the source-to-detector distance was set to the maximum of the system).

While the time taken to compute a full performance map is acceptable for establishing a comprehensive understanding of the spatial variability of the inspection performance, a simplified computation is required to quickly assess new proposed setups within the optimisation loop. In this case, 7 positions were picked to evenly cover the bracket zone (highlighted in yellow in Fig. 50(b)). For each proposed setup, the same workflow outlined in Fig. 51 was used to compute performance metrics across all 7 positions, which were then averaged to create a single objective metric for the optimiser. In this case, each evaluation required approximately 100 s. Depending on the setups being proposed, some defect indications may lie outside the field of view of the scan for some projections, which can be easily detected using the known spatial mapping between the setup space, the detector space, and the reconstructed volume space. In these cases, these evaluations were skipped over without simulation. The final simplex used by the Nelder–Mead optimiser spanned less than 0.5 degrees across the rotational parameters, less than 0.5 mm in the translational offsets, and approximately 1 mm for the source-to-object distance parameter.

The best setup found is shown in Fig. 52. The inspection performance metrics before and after the optimisation are presented in

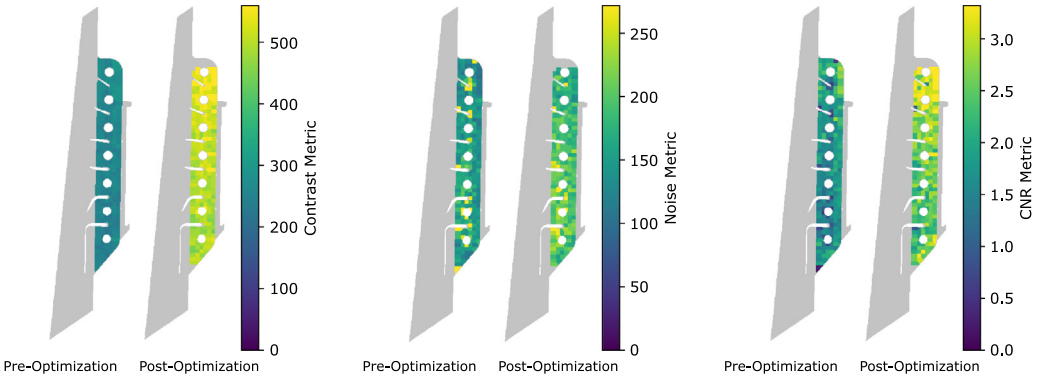

Fig. 53. The performance metrics for the part bracket pre- and post-optimisation. A drastic improvement of the contrast metric was seen, with only minor changes seen in the noise metric. The result for the CNR metric is significantly improved across the bracket after the optimisation.

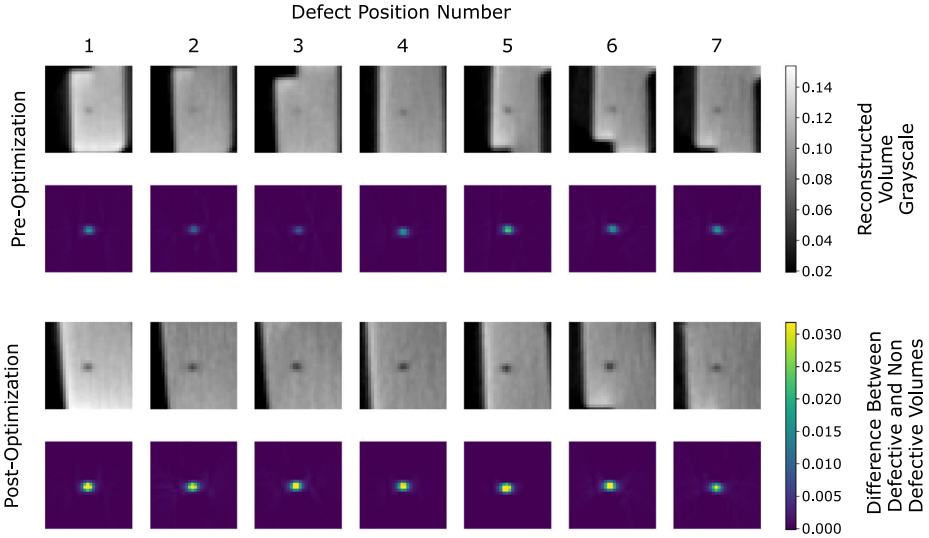

Fig. 54. Defect indications for the seven positions before and after optimisation. The greyscale range used for plotting is identical across all of the reconstructed volume patches. The greyscale range used for plotting the difference volume patches is also identical across all different images. .

Fig. 53, where it can be seen that the calculated performance has improved considerably. Fig. 54 shows defect indications evaluated at each position, where it can be seen that the defect indications appear significantly improved, both in magnification and contrast.

The most notable change between the initial and optimised setup is that the magnification has been increased to focus the scan on the bracket section. Additionally, the aerofoil has been tilted slightly, which explores the trade-off of incurring slightly longer material path lengths across the part (reducing performance), at the benefit of reducing the vertical extent of the bracket to increase magnification (increasing performance). It can be seen that the tip section of the bracket region lies outside of the scan. This is because the optimiser did not check that all parts of the bracket were in the field of view (only the 7 positions were checked) but in future, more points along the outer extent of the region of interest should be factored into this field of view check.

11. Conclusion

This paper presented gVXR, an open-source framework for simulating X-ray images in real time using GPUs. We have demonstrated gVXR's versatility and applicability across various domains, including education, experimental setup optimisation, digital twinning, machine learning, non-destructive testing, and materials science. Extensive validation efforts, including comparisons with Monte Carlo simulations and real experimental data, have confirmed the accuracy of gVXR's simulations. The framework's ability to rapidly generate verifiably accurate X-ray simulations enables researchers and practitioners to explore complex scenarios, optimise experimental parameters, and develop novel approaches in X-ray imaging and analysis. As gVXR continues to evolve, potential areas for future development include improved scatter estimation and enhanced support for spectral imaging. The open-source nature of gVXR enables collaboration and innovation, encouraging future advancements in X-ray simulation and analysis across multiple disciplines.

Acronyms

2D	two-dimensional
3D	three-dimensional
AM	additive manufacturing
API	application programming interface
CAD	computer-aided design
CBCT	cone-beam computed tomography
CG	computer graphics
CIL	Core Imaging Library

CMA-ES	covariance matrix adaptation evolution strategy
CNN	convolutional neural network
CNR	contrast-to-noise ratio
CPU	central processor unit
CSG	Constructive Solid Geometry
CT	computed tomography
DIAD	Dual Imaging And Diffraction
DL	deep learning
DLS	Diamond Light Source
DR	digital radiograph
DRAMA	Digital Reconfigurable Additive Manufacturing facilities for Aerospace
DRR	digitally reconstructed radiograph
ERROR	pEdiatRic dosimetRy personalised platfORm
eV	electronvolt
FBP	filtered-back projection
FML	fibre-metal laminate
GPU	graphics processor unit
GUI	graphical user interface
gVXR	gVirtualXray
ITK	Insight Toolkit
keV	kiloelectronvolt
kVp	kilovoltage peak
labCT	laboratory computed tomography
LSF	line spread-function
MAPE	mean absolute percentage error
mAs	milliampere-second
MC	Monte Carlo
MEng	Master of Engineering
MeV	megaelectronvolt
ML	machine learning
MRI	magnetic resonance imaging
MSE	mean squared error
NDT	non-destructive testing
PrePREG	PREimPREGnated
PSF	point spread function
PTC	percutaneous transhepatic cholangiography
RA	rheumatoid arthritis
RMSE	root mean squared error
SDD	source-to-detector distance
SIRT	Simultaneous Iterations Reconstruction Technique
SOD	source-to-object distance
SSIM	structural similarity index
TV	total variation
VR	virtual reality
VTK	Visualisation Toolkit
XCT	X-ray computed tomography
ZNCC	zero-mean normalised cross-correlation
ZrB_2	zirconium diboride
ZrO_2	zirconium dioxide

Declaration of competing interest

The authors declare that they have no known competing financial interests or personal relationships that could have appeared to influence the work reported in this paper.

Acknowledgements

gVirtualXray is currently supported by the Ada Lovelace Centre and the UKRI Digital Research Infrastructure Programme through the Science and Technology Facilities Council's Computational Science Centre for Research Communities (CoSeC). It was initially co-funded by the European Union through the FP7-PEOPLE-2012-CIG - Marie-Curie Action 'Fly Algorithm in PET Reconstruction for Radiotherapy Treatment Planning' under grant # 321968 and by the Welsh government through the Research Institute of Visual Computing (RIVIC). F. Vidal thanks NVIDIA Corporation for the donation of the NVIDIA TITAN Xp GPU used in the development and validation of gVirtualXray. I. Mitchell is supported through the UKRI CDT in Artificial Intelligence, Machine Learning and Advanced Computing (AIMLAC - EP/S023992/1). F. Vidal, I. Mitchell and S. Middleburgh acknowledge the Diamond Light Source for beamtime # MG29820 on 'Real experiments, hi-fidelity simulations, machine learning and GPUs: Toward the virtual design of nuclear fuel rods'. I. Mitchell and F. Vidal would like to thank Taith for a travel grant awarded to Vidal and Mitchell that made it possible to develop the digital twin of the new dual-beam XRCT laboratory equipment of the MateIS laboratory (Lyon, France). Y. Chahid and C. Atkins acknowledge the UKRI Future Leaders Fellowship 'Printing the future of space telescopes' under grant # MR/T042230/1. J. Friemann acknowledges funding from Horizon Europe through the MSCA Doctoral Network RELIANCE, grant # 101073040. A. Garbout, M. Puig, and H. Lipscomb acknowledges support from the National Research Facility for Lab X-ray CT (NXCT), funded through EPSRC grants # EP/T02593X/1 and # EP/V035932/1 R. Culver acknowledges the 'DRAMA (Digital Reconfigurable Additive Manufacturing facilities for Aerospace)' project funded by UKRI under grant # 113157. A. Rouwane, C. Michelet, J.-F. Giovannelli, P. Desbarats, and H. Seznec acknowledges support from the *Agence Nationale de la Recherche* (ANR CES2010, no. CESA 009 01, TITANIUMS), and the *Région Aquitaine* (TOX-NANO no. 20111201003/POPRA no. 14006636-034). A. Rouwane's postdoctoral fellowship is funded by the "Exploratory Interdisciplinary Research" program of the *Université de Bordeaux* (SHAPE Project, LP2IB, LaBRI, IMS). E. Béchet and C. Leblanc thank the Walloon Region for its support under grant no. 8424 "AEROCT".

References

[1] P. Duvauchelle, N. Freud, V. Kaftandjian, D. Babot, A computer code to simulate X-ray imaging techniques, Nucl. Instrum. Methods Phys. Res. Sect. B: Beam Interact. Mater. Atoms 170 (1) (2000) 245–258, http://dx.doi.org/10.1016/S0168-583X(00)00185-3.

[2] F.P. Vidal, M. Garnier, N. Freud, J.M. Létang, N.W. John, Simulation of X-ray attenuation on the GPU, in: Proceedings of Theory and Practice of Computer Graphics 2009, Eurographics Association, Cardiff, UK, 2009, pp. 25–32, http://dx.doi.org/10.2312/LocalChapterEvents/TPCG/TPCG09/025-032.

[3] F.P. Vidal, P.-F. Villard, Development and validation of real-time simulation of X-ray imaging with respiratory motion, Comput. Med. Imaging Graph. 49 (2016) 1–15, http://dx.doi.org/10.1016/j.compmedimag.2015.12.002.

[4] N. Freud, P. Duvauchelle, J.M. Létang, D. Babot, Fast and robust ray casting algorithms for virtual X-ray imaging, Nucl. Instrum. Methods Phys. Res. Sect. B: Beam Interact. Mater. Atoms 248 (1) (2006) 175–180, http://dx.doi.org/10.1016/j.nimb.2006.03.009.

[5] P.-F. Villard, F.P. Vidal, C. Hunt, F. Bello, N.W. John, S. Johnson, D.A. Gould, A prototype percutaneous transhepatic cholangiography training simulator with real-time breathing motion, Int. J. Comput. Assist. Radiol. Surg. 4 (6) (2009) 571–578, http://dx.doi.org/10.1007/s11548-009-0367-1.

[6] F.P. Vidal, M. Garnier, N. Freud, J.M. Létang, N.W. John, Accelerated Deterministic Simulation of X-ray Attenuation Using Graphics Hardware, in: A. Hast, I. Viola (Eds.), Eurographics 2010 - Posters, The Eurographics Association, Norrköping, Sweden, 2010, http://dx.doi.org/10.2312/egp.20101026, Poster 5011.

[7] F.P. Vidal, I.T. Mitchell, J.M. Létang, Use of fast realistic simulations on GPU to extract CAD models from microtomographic data in the presence of strong CT artefacts, Precis. Eng. 74 (2022) 110–125, http://dx.doi.org/10.1016/j.precisioneng.2021.10.014.

[8] J.L. Pointon, T. Wen, J. Tugwell-Allsup, A. Sújar, J.M. Létang, F.P. Vidal, Simulation of X-ray projections on GPU: Benchmarking gVirtualXray with clinically realistic phantoms, Comput. Methods Programs Biomed. 234 (2023) 107500, http://dx.doi.org/10.1016/j.cmpb.2023.107500.

[9] A. Corbi, D. Burgos, F. Vidal, F. Albiol, A. Albiol, X-ray imaging virtual online laboratory for engineering undergraduates, Eur. J. Phys. 41 (1) (2019) 014001, http://dx.doi.org/10.1088/1361-6404/ab5011.

[10] T. Schoonjans, A. Brunetti, B. Golosio, M. Sanchez del Rio, V.A. Solé, C. Ferrero, L. Vincze, The xraylib library for X-ray–matter interactions. recent developments, Spectrochim. Acta Part B: At. Spectrosc. 66 (11) (2011) 776–784, http://dx.doi.org/10.1016/j.sab.2011.09.011.

[11] G. Poludniowski, A. Omar, R. Bujila, P. Andreo, Technical note: Spekpy v2.0—a software toolkit for modeling X-ray tube spectra, Med. Phys. 48 (7) (2021) 3630–3637, http://dx.doi.org/10.1002/mp.14945.

[12] G. Hernández, F. Fernández, A model of tungsten anode X-ray spectra, Med. Phys. 43 (8Part1) (2016) 4655–4664, http://dx.doi.org/10.1118/1.4955120.

[13] Z. Gao, H. Lan, C. Zhang, Y. Huang, J. Fu, Modeling technique for optimizing simulation objective function based on key parameters of the X-ray imaging system, in: Proceedings of the 2024 7th International Conference on Machine Vision and Applications, ICMVA '24, Association for Computing Machinery, New York, NY, USA, 2024, pp. 139–144, http://dx.doi.org/10.1145/3653946.3653967.

[14] D. Ou, Y. Xiao, D. Lan, Y. Wang, Type a standard uncertainty evaluation in one measurement through uncertainty propagation from voxel values' distribution for computed tomography metrology, Meas. Sci. Technol. 35 (6) (2024) 065015, http://dx.doi.org/10.1088/1361-6501/ad30ba.

[15] V. Scarponi, J. Verde, N. Haouchine, M. Duprez, F. Nageotte, S. Cotin, FBG-driven simulation for virtual augmentation of fluoroscopic images during endovascular interventions, Heal. Technol. Lett. (2025) http://dx.doi.org/10.1049/htl2.12108.

[16] J.S. Jørgensen, E. Ametova, G. Burca, G. Fardell, E. Papoutsellis, E. Pasca, K. Thielemans, M. Turner, R. Warr, W.R.B. Lionheart, P.J. Withers, Core Imaging Library - Part I: a versatile Python framework for tomographic imaging, Philos. Trans. R. Soc. A: Math. Phys. Eng. Sci. 379 (2204) (2021) 20200192, http://dx.doi.org/10.1098/rsta.2020.0192.

[17] P. Papadimitroulas, W.D. Erwin, V. Iliadou, T. Kostou, G. Loudos, G.C. Kagadis, A personalized, Monte Carlo-based method for internal dosimetric evaluation of radiopharmaceuticals in children, Med. Phys. 45 (8) (2018) 3939–3949, http://dx.doi.org/10.1002/mp.13055.

[18] S. Rodriguez Perez, N. Marshall, L. Struelens, H. Bosmans, Characterization and validation of the thorax phantom lungman for dose assessment in chest radiography optimization studies, J. Med. Imaging 5 (2018) 1, http://dx.doi.org/10.1117/1.JMI.5.1.013504.

[19] M. McCormick, X. Liu, L. Ibanez, J. Jomier, C. Marion, ITK: enabling reproducible research and open science, Front. Neuroinform. 8 (2014) 13, http://dx.doi.org/10.3389/fninf.2014.00013.

[20] W. Schroeder, K. Martin, B. Lorensen, The Visualization Toolkit – An Object-Oriented Approach To 3D Graphics, Fourth, Kitware, Inc., 2006.

[21] F.P. Vidal, J. Tugwell-Allsup, CT scans, 3D segmentations, digital radiograph and 3D surfaces of the Lungman phantom, Zenodo, 2024, http://dx.doi.org/10.5281/zenodo.10782644.

[22] W. Schneider, T. Bortfeld, W. Schlegel, Correlation between CT numbers and tissue parameters needed for Monte Carlo simulations of clinical dose distributions, Phys. Med. Biol. 45 (2) (2000) 459–478, http://dx.doi.org/10.1088/0031-9155/45/2/314.

[23] M. Vestbøstad, K. Karlgren, N.R. Olsen, Research on simulation in radiography education: a scoping review protocol, Syst. Rev. 9 (263) (2020) http://dx.doi.org/10.1186/s13643-020-01531-2.

[24] A. Partner, N. Shiner, E. Hyde, S. Errett, First year student radiographers' perceptions of a one-week simulation-based education package designed to increase clinical placement capacity, Radiography 28 (3) (2022) 577–585, http://dx.doi.org/10.1016/j.radi.2022.04.007.

[25] Ionising Radiation (Medical Exposure) (Amendment) Regulations 2024, vol. 896, 2024, (Accessed 18 Dcember 2024).

[26] Z. Zuo, W.Y. Qian, X. Liao, P.-A. Heng, Position based catheterization and angiography simulation, in: 2018 IEEE 6th International Conference on Serious Games and Applications for Health, SeGAH, 2018, pp. 1–7, http://dx.doi.org/10.1109/SeGAH.2018.8401369.

[27] X. Xu, A. Puggioni, D. Kilroy, A.G. Campbell, Mixed reality and real-time X-Ray simulation in vet radiography training: A user-centered comparative study, in: 2025 IEEE Conference Virtual Reality and 3D User Interfaces, VR, 2025, pp. 12–22, http://dx.doi.org/10.1109/VR59515.2025.00026.

[28] M. Racy, A. Barrow, J. Tomlinson, F. Bello, Development and validation of a virtual reality haptic femoral nailing simulator, J. Surg. Educ. 78 (3) (2021) 1013–1023, http://dx.doi.org/10.1016/j.jsurg.2020.10.004.

[29] L. Dixon, XRayViewer - A C++ Unreal Engine 5 Wrapper for gVirtualXRay, Bangor University, 2022.

[30] A. Sujar, G. Kelly, M. García, F.P. Vidal, Interactive teaching environment for diagnostic radiography with real-time X-ray simulation and patient positioning, Int. J. Comput. Assist. Radiol. Surg. 17 (1) (2022) 85–95, http://dx.doi.org/10.1007/s11548-021-02499-7.

[31] S. Agostinelli, J. Allison, K. Amako, J. Apostolakis, H. Araujo, P. Arce, M. Asai, D. Axen, S. Banerjee, G. Barrand, F. Behner, L. Bellagamba, J. Boudreau, L. Broglia, A. Brunengo, H. Burkhardt, S. Chauvie, J. Chuma, R. Chytracek, G. Cooperman, G. Cosmo, P. Degtyarenko, A. Dell'Acqua, G. Depaola, D. Dietrich, R. Enami, A. Feliciello, C. Ferguson, H. Fesefeldt, G. Folger, F. Foppiano, A. Forti, S. Garelli, S. Giani, R. Giannitrapani, D. Gibin, J. Gómez Cadenas, I. González, G. Gracia Abril, G. Greeniaus, W. Greiner, V. Grichine, A. Grossheim, S. Guatelli, P. Gumplinger, R. Hamatsu, K. Hashimoto, H. Hasui, A. Heikkinen, A. Howard, V. Ivanchenko, A. Johnson, F. Jones, J. Kallenbach, N. Kanaya, M. Kawabata, Y. Kawabata, M. Kawaguti, S. Kelner, P. Kent, A. Kimura, T. Kodama, R. Kokoulin, M. Kossov, H. Kurashige, E. Lamanna, T. Lampén, V. Lara, V. Lefebure, F. Lei, M. Liendl, W. Lockman, F. Longo, S. Magni, M. Maire, E. Medernach, K. Minamimoto, P. Mora de Freitas, Y. Morita, K. Murakami, M. Nagamatu, R. Nartallo, P. Nieminen, T. Nishimura, K. Ohtsubo, M. Okamura, S. O'Neale, Y. Oohata, K. Paech, J. Perl, A. Pfeiffer, M. Pia, F. Ranjard, A. Rybin, S. Sadilov, E. Di Salvo, G. Santin, T. Sasaki, N. Savvas, Y. Sawada, S. Scherer, S. Sei, V. Sirotenko, D. Smith, N. Starkov, H. Stoecker, J. Sulkimo, M. Takahata, S. Tanaka, E. Tcherniaev, E. Safai Tehrani, M. Tropeano, P. Truscott, H. Uno, L. Urban, P. Urban, M. Verderi, A. Walkden, W. Wander, H. Weber, J. Wellisch, T. Wenaus, D. Williams, D. Wright, T. Yamada, H. Yoshida, D. Zschiesche, Geant4—a simulation toolkit, Nucl. Instrum. Methods Phys. Res. Sect. A: Accel. Spectrometers Detect. Assoc. Equip. 506 (3) (2003) 250–303, http://dx.doi.org/10.1016/S0168-9002(03)01368-8.

[32] S. Rit, M.V. Oliva, S. Brousmiche, R. Labarbe, D. Sarrut, G.C. Sharp, The reconstruction toolkit (RTK), an open-source cone-beam ct reconstruction toolkit based on the insight toolkit (ITK), J. Phys.: Conf. Ser. 489 (1) (2014) 012079, http://dx.doi.org/10.1088/1742-6596/489/1/012079.

[33] E. Maire, G. Bonnard, J. Adrien, X. Boulnat, J.M. Létang, J. Lachambre, Dual beam microfocus high-energy tomography: Towards multimodal and faster laboratory experiments, Tomogr. Mater. Struct. 5 (2024) 100030, http://dx.doi.org/10.1016/j.tmater.2024.100030.

[34] J.M. Létang, J. Lachambre, É. Maire, Cross-detector scatter issues in dual synchronous tomography: an affine projection correction protocol, Tomogr. Mater. Struct. 6 (2024) 100039, 10.1016/j.tmater.2024.100039.

[35] C. Reinhard, M. Drakopoulos, S.I. Ahmed, H. Deyhle, A. James, C.M. Charlesworth, M. Burt, J. Sutter, S. Alexander, P. Garland, T. Yates, R. Marshall, B. Kemp, E. Warrick, A. Pueyos, B. Bradnick, M. Nagni, A.D. Winter, J. Filik, M. Basham, N. Wadeson, O.N.F. King, N. Aslani, A.J. Dent, Beamline K11 DIAD: a new instrument for dual imaging and diffraction at Diamond Light Source, J. Synchrotron Radiat. 28 (6) (2021) 1985–1995, http://dx.doi.org/10.1107/S1600577521009875.

[36] I.T. Mitchell, J.M. Létang, L.M. Evans, F.P. Vidal, WebCT – OpenSource web-based GUI for real-time X-ray simulation, Tomogr. Mater. Struct. 8 (2025) http://dx.doi.org/10.1016/j.tmater.2025.100057.

[37] F. Albiol, A. Corbi, A. Albiol, Densitometric radiographic imaging with contour sensors, IEEE Access 7 (2019) 18902–18914, http://dx.doi.org/10.1109/ACCESS.2019.2895925.

[38] A. Corbi, Environment recognition applied to particle detectors (Ph.D. thesis), University of Valencia, Valencia, Spain, 2017, URL https://digital.csic.es/bitstream/10261/225165/1/Corbi_Bellot.pdf.

[39] WormAtlas: A database featuring behavioral and structural anatomy of Caenorhabditis elegans, 2024, https://www.wormatlas.org/. (Accessed 18 December 2024).

[40] Spatial transcriptomics of C. elegans males and hermaphrodites, 2024, http://celegans.tomoseq.genomes.nl/. (Accessed 18 December 2024).

[41] WormBook: The online review of C. elegans biology, 2024, http://www.wormbook.org/. (Accessed 18 December 2024).

[42] C. Michelet, P. Barberet, P. Desbarats, J.-F. Giovannelli, C. Schou, I. Chebil, M.-H. Delville, N. Gordillo, D.G. Beasley, G. Devès, et al., An implementation of the NiftyRec medical imaging library for PIXE-tomography reconstruction, Nucl. Instrum. Methods Phys. Res. Sect. B: Beam Interact. Mater. Atoms 404 (2017) 131–139, http://dx.doi.org/10.1016/j.nimb.2017.01.067.

[43] G. McColl, S.A. James, S. Mayo, D.L. Howard, C.G. Ryan, R. Kirkham, G.F. Moorhead, D. Paterson, M.D. De Jonge, A.I. Bush, Caenorhabditis elegans maintains highly compartmentalized cellular distribution of metals and steep concentration gradients of manganese, PLoS One 7 (2) (2012) e32685, http://dx.doi.org/10.1371/journal.pone.0032685.

[44] Q. Le Trequesser, G. Saez, G. Devès, C. Michelet, P. Barberet, M.-H. Delville, H. Seznec, In situ titanium dioxide nanoparticles quantitative microscopy in cells and inC. elegans using nuclear microprobe analysis, Nucl. Instrum. Methods Phys. Res. Sect. B: Beam Interact. Mater. Atoms 341 (2014) 58–64, http://dx.doi.org/10.1016/j.nimb.2014.06.031.

[45] L.M. Rossbach, D.A. Brede, G. Nuyts, S. Cagno, R.M.S. Olsson, D.H. Oughton, G. Falkenberg, K. Janssens, O.C. Lind, Synchrotron XRF analysis identifies cerium accumulation colocalized with pharyngeal deformities in CeO_2 NP-exposed Caenorhabditis elegans, Environ. Sci. Technol. 56 (8) (2022) 5081–5089, http://dx.doi.org/10.1021/acs.est.1c08509.s001.

[46] C. Michelet, P. Barberet, P. Moretto, H. Seznec, Development and applications of STIM- and PIXE-tomography: A review, Nucl. Instrum. Methods Phys. Res. Sect. B: Beam Interact. Mater. Atoms 363 (2015) 55–60, http://dx.doi.org/10.1016/j.nimb.2015.08.070.

[47] K.H. Jin, M.T. McCann, E. Froustey, M. Unser, Deep convolutional neural network for inverse problems in imaging, IEEE Trans. Image Process. 26 (9) (2017) 4509–4522, http://dx.doi.org/10.1109/tip.2017.2713099.

[48] K. Matsubara, M. Ibaraki, M. Nemoto, H. Watabe, Y. Kimura, A review on AI in PET imaging, Ann. Nucl. Med. 36 (2) (2022) 133–143, http://dx.doi.org/10.1007/s12149-021-01710-8.

[49] B. Szigeti, P. Gleeson, M. Vella, S. Khayrulin, A. Palyanov, J. Hokanson, M. Currie, M. Cantarelli, G. Idili, S. Larson, OpenWorm: an open-science approach to modeling Caenorhabditis elegans, Front. Comput. Neurosci. 8 (2014) 137, http://dx.doi.org/10.3389/fncom.2014.00137.

[50] P.W. Sternberg, K. Van Auken, Q. Wang, A. Wright, K. Yook, M. Zarowiecki, V. Arnaboldi, A. Becerra, S. Brown, S. Cain, et al., WormBase 2024: status and transitioning to Alliance infrastructure, Genetics 227 (1) (2024) iyae050, http://dx.doi.org/10.1093/genetics/iyae050.

[51] The Virtual Worm Project, 2024, http://caltech.wormbase.org/virtualworm/. (Accessed 18 December 2024).

[52] W. Van Aarle, W.J. Palenstijn, J. Cant, E. Janssens, F. Bleichrodt, A. Dabravolski, J. De Beenhouwer, K. Joost Batenburg, J. Sijbers, Fast and flexible X-ray tomography using the ASTRA toolbox, Opt. Express 24 (22) (2016) 25129–25147, http://dx.doi.org/10.1364/oe.24.025129.

[53] L. Mishnaevsky Jr., Sustainable end-of-life management of wind turbine blades: Overview of current and coming solutions, Materials 14 (5) (2021) 1124, http://dx.doi.org/10.3390/ma14051124.

[54] H. Lee, Y.M. Hwang, J. Lee, N.-W. Kim, S.-K. Ko, A drone-driven X-Ray image-based diagnosis of wind turbine blades for reliable operation of wind turbine, IEEE Access 12 (2024) 56141–56158, http://dx.doi.org/10.1109/ACCESS.2024.3388494.

[55] F.P. Vidal, P.-F. Villard, Simulated motion artefact in computed tomography, in: K. Bühler, L. Linsen, N.W. John (Eds.), Eurographics Workshop on Visual Computing for Biology and Medicine, The Eurographics Association, 2015, pp. 213–214, http://dx.doi.org/10.2312/vcbm.20151228.

[56] S.F. Gibson, 3D chainmail: a fast algorithm for deforming volumetric objects, in: Proceedings of the 1997 Symposium on Interactive 3D Graphics, in: I3D '97, Association for Computing Machinery, New York, NY, USA, 1997, pp. 149–ff., http://dx.doi.org/10.1145/253284.253324, URL.

[57] J. Lovitt, Estimating length statistics of aggregate fried potato product via electromagnetic radiation attenuation, 2016, URL https://scholarworks.boisestate.edu/td/1211.

[58] M. Haiderbhai, S. Ledesma, S.C. Lee, M. Seibold, P. Fürnstahl, N. Navab, P. Fallavollita, Pix2xray: converting RGB images into X-rays using generative adversarial networks, Int. J. Comput. Assist. Radiol. Surg. 15 (6) (2020) 973–980, http://dx.doi.org/10.1007/s11548-020-02159-2.

[59] E. Andreozzi, A. Fratini, D. Esposito, M. Cesarelli, P. Bifulco, Toward a priori noise characterization for real-time edge-aware denoising in fluoroscopic devices, BioMedical Eng. OnLine 20 (1) (2021) 36, http://dx.doi.org/10.1186/s12938-021-00874-8.

[60] G. Litjens, T. Kooi, B.E. Bejnordi, A.A.A. Setio, F. Ciompi, M. Ghafoorian, J.A. Van Der Laak, B. Van Ginneken, C.I. Sánchez, A survey on deep learning in medical image analysis, Med. Image Anal. 42 (2017) 60–88, http://dx.doi.org/10.1016/j.media.2017.07.005.

[61] F. Garcea, A. Serra, F. Lamberti, L. Morra, Data augmentation for medical imaging: A systematic literature review, Comput. Biol. Med. 152 (2023) 106391, http://dx.doi.org/10.1016/j.compbiomed.2022.106391.

[62] R. Osuala, K. Kushibar, L. Garrucho, A. Linardos, Z. Szafranowska, S. Klein, B. Glocker, O. Diaz, K. Lekadir, Data synthesis and adversarial networks: A review and meta-analysis in cancer imaging, Med. Image Anal. 84 (2023) 102704, http://dx.doi.org/10.1016/j.media.2022.102704.

[63] A. Phoulady, Y. Suleiman, H. Choi, T. Moore, N. May, S. Shahbazmohamadi, P. Tavousi, Synthetic data augmentation to enhance manual and automated defect detection in microelectronics, Microelectron. Reliab. 150 (2023) 115220, http://dx.doi.org/10.1016/j.microrel.2023.115220, Special issue of 34th European Symposium on Reliability of Electron Devices, Failure Physics and Analysis, ESREF 2023.

[64] G. Kervyn, The First Open Source 3d Atlas of Human Anatomy, Acta Sci. Anat. 1 (4) (2022) 13–15.

[65] Home of the Blender project - Free and Open 3D Creation Software, 2024, https://www.blender.org/. (Accessed 18 December 2024).

[66] J. Valentin (Ed.), Basic Anatomical and Physiological Data for Use in Radiological Protection: Reference Values, Annals of the ICRP, (32,3/4) Pergamon Press, Oxford, 2003.

[67] G. Jocher, A. Chaurasia, J. Qiu, Ultralytics YOLO (Version 8.0.0) [Computer software], 2023, URL https://github.com/ultralytics/ultralytics.

[68] E. Sogancioglu, B.V. Ginneken, F. Behrendt, M. Bengs, A. Schlaefer, M. Radu, D. Xu, K. Sheng, F. Scalzo, E. Marcus, S. Papa, J. Teuwen, E.T. Scholten, S. Schalekamp, N. Hendrix, C. Jacobs, W. Hendrix, C.I. Sánchez, K. Murphy, Nodule Detection and Generation on Chest X-Rays: NODE21 Challenge, IEEE Trans. Med. Imaging 43 (8) (2024) 2839–2853, http://dx.doi.org/10.1109/TMI.2024.3382042, URL https://ieeexplore.ieee.org/document/10479589/.

[69] J. Friemann, L.P. Mikkelsen, C. Oddy, M. Fagerström, Automated generation of labeled synthetic training data for machine learning based segmentation of 3D-woven composites, in: Proceedings of the 21st European Conference on Composite Materials: Special Sessions, vol. 8, 2024, pp. 333–338, http://dx.doi.org/10.60691/yj56-np80.

[70] L. Brown, A. Long, 8 - modeling the geometry of textile reinforcements for composites: TexGen, in: P. Boisse (Ed.), Composite Reinforcements for Optimum Performance (Second Edition), second ed., in: Woodhead Publishing Series in Composites Science and Engineering, Woodhead Publishing, 2021, pp. 237–265, http://dx.doi.org/10.1016/B978-0-12-819005-0.00008-3.

[71] S. Bosse, GitHub - bslab/XraySim: Radiography and CT xray simulator and parallel filtered back projection — github.com, 2024, https://github.com/bslab/xraysim. (Accessed 18 December 2024).

[72] S. Bosse, D. Lehmhus, S. Kumar, Automated porosity characterization for aluminum die casting materials using X-ray radiography, synthetic X-ray data augmentation by simulation, and machine learning, Sensors 24 (9) (2024) 2933, http://dx.doi.org/10.3390/s24092933.

[73] Y. Zhang, Z. Shen, R. Jiao, Segment anything model for medical image segmentation: Current applications and future directions, Comput. Biol. Med. (2024) 108238, http://dx.doi.org/10.1016/j.compbiomed.2024.108238.

[74] GitHub - facebookresearch/detectron2: Detectron2 is a platform for object detection, segmentation and other visual recognition tasks. — github.com, 2024, https://github.com/facebookresearch/detectron2. (Accessed 18 December 2024).

[75] OpenSCAD the programmers solid 3D CAD modeller, 2024, https://openscad.org/. (Accessed 18 December 2024).

[76] C. Shah, S. Bosse, A. von Hehl, Taxonomy of damage patterns in composite materials, measuring signals, and methods for automated damage diagnostics, Materials 15 (13) (2022) 4645, http://dx.doi.org/10.3390/ma15134645.

[77] D.-H. Yang, J.-Y. Huang, J.-Y. Chiou, J.C.-C. Wei, Analysis of socioeconomic status in the patients with rheumatoid arthritis, Int. J. Environ. Res. Public Heal. 15 (6) (2018) 1194, http://dx.doi.org/10.3390/ijerph15061194.

[78] R.P. Mihail, N. Jacobs, J. Goldsmith, K. Lohr, Serious games analytics: Methodologies for performance measurement, assessment, and improvement, Springer International Publishing, Cham, 2015, pp. 211–231, http://dx.doi.org/10.1007/978-3-319-05834-4_9.

[79] T. Wen, R. Mihail, s. Al-maliki, J. Letang, F. Vidal, Registration of 3D triangular models to 2D X-ray projections using black-box optimisation and X-ray simulation, in: F.P. Vidal, G.K.L. Tam, J.C. Roberts (Eds.), Computer Graphics and Visual Computing, CGVC, The Eurographics Association, 2019, pp. 105–113, http://dx.doi.org/10.2312/cgvc.20191265.

[80] T. Wen, R.P. Mihail, F.P. Vidal, 3D-2d registration using X-ray simulation and CMA-ES, in: P.A. Castillo, J.L. Jiménez Laredo (Eds.), Applications of Evolutionary Computation, Springer International Publishing, Cham, 2021, pp. 453–468, http://dx.doi.org/10.1007/978-3-030-72699-7_29.

[81] H. Toda, X-Ray CT - Hardware and Software Techniques, Springer, Singapore, 2021, http://dx.doi.org/10.1007/978-981-16-0590-1, URL https://link.springer.com/10.1007/978-981-16-0590-1.

[82] N. Uhlman, M. Salamon, S. Burtzlaff, Components and Methods for Highest Resolution Computed Tomography, International Symposium on NDT in Aerospace (Fürth, Germany), vol. 1 (2008) 3–9.

[83] G. Kerckhofs, G. Pyka, M. Moesen, S. Van Bael, J. Schrooten, M. Wevers, High-Resolution Microfocus X-Ray Computed Tomography for 3D Surface Roughness Measurements of Additive Manufactured Porous Materials, Adv. Eng. Mater. 15 (3) (2013) 153–158, http://dx.doi.org/10.1002/adem.201200156, URL https://onlinelibrary.wiley.com/doi/10.1002/adem.201200156.

[84] Y. Nikishkov, G. Seon, A. Makeev, Structural analysis of composites with porosity defects based on X-ray computed tomography, J. Compos. Mater. 48 (17) (2014) 2131–2144, http://dx.doi.org/10.1177/0021998313494917.

[85] M. Makarkin, D. Bratashov, State-of-the-art approaches for image deconvolution problems, including modern deep learning architectures, Micromachines 12 (12) (2021) http://dx.doi.org/10.3390/mi12121558.

[86] J. Zhu, K. Li, B. Hao, Hybrid variational model based on alternating direction method for image restoration, Adv. Difference Equ. 2019 (1) (2019) http://dx.doi.org/10.1186/s13662-018-1908-0.

[87] P. Wu, J.M. Boone, A.M. Hernandez, M. Mahesh, J.H. Siewerdsen, Theory, method, and test tools for determination of 3D MTF characteristics in cone-beam CT, Med. Phys. 48 (6) (2021) 2772–2789, http://dx.doi.org/10.1002/mp.14820.

[88] I.A. Cunningham, B.K. Reid, Signal and noise in modulation transfer function determinations using the slit, wire, and edge techniques, Med. Phys. 19 (4) (1992) 1037–1044, http://dx.doi.org/10.1118/1.596821.

[89] J.M. Létang, G. Peix, On-line X-ray focal spot assessment based on deconvolution using standard imaging devices, NDT E Int. 36 (5) (2003) 303–317, http://dx.doi.org/10.1016/S0963-8695(03)00010-0.

[90] L. Shi, N.R. Bennett, A.S. Wang, Characterization of x-ray focal spots using a rotating edge, J. Med. Imaging 8 (2) (2021) 023502, http://dx.doi.org/10.1117/1.JMI.8.2.023502.

[91] Z. Chen, R. Ning, Three-dimensional point spread function measurement of cone-beam computed tomography system by interactive edge-blurring algorithm, Phys. Med. Biol. 49 (10) (2004) 1865–1880, http://dx.doi.org/10.1088/0031-9155/49/10/003.

[92] M.M. Thornton, M.J. Flynn, Measurement of the spatial resolution of a clinical volumetric computed tomography scanner using a sphere phantom, in: M.J. Flynn, J. Hsieh (Eds.), in: Medical Imaging 2006: Physics of Medical Imaging, vol. 6142, International Society for Optics and Photonics. SPIE, 2006, p. 61421Z, http://dx.doi.org/10.1117/12.654969.

[93] C. Lee, J. Baek, A new method to measure directional modulation transfer function using sphere phantoms in a cone beam computed tomography system, IEEE Trans. Med. Imaging 34 (4) (2015) 902–910, http://dx.doi.org/10.1109/TMI.2014.2369524.

[94] N. Robert, J.G. Mainprize, C. Whyne, Determination of 3D PSFs from computed tomography reconstructed x-ray images of spherical objects and the effects of sphere radii, Med. Phys. 46 (11) (2019) 4792–4802, http://dx.doi.org/10.1002/mp.13734.

[95] C. Lee, H. dong Song, J. Baek, 3D MTF estimation using sphere phantoms for cone-beam computed tomography systems, Med. Phys. 47 (7) (2020) 2838–2851, http://dx.doi.org/10.1002/mp.14147.

[96] P. Russo, G. Mettivier, Method for measuring the focal spot size of an x-ray tube using a coded aperture mask and a digital detector, Med. Phys. 38 (4) (2011) 2099–2115, http://dx.doi.org/10.1118/1.3567503.

[97] S.N. Friedman, G.S. Fung, J.H. Siewerdsen, B.M. Tsui, A simple approach to measure computed tomography (CT) modulation transfer function (MTF) and noise-power spectrum (NPS) using the American College of Radiology (ACR) accreditation phantom, Med. Phys. 40 (5) (2013) 1–9, http://dx.doi.org/10.1118/1.4800795.

[98] G.M. Probst, Q. Hou, B. Boeckmans, Y.S. Xiao, W. Dewulf, Characterization and stability monitoring of X-ray focal spots, CIRP Ann 69 (1) (2020) 453–456, http://dx.doi.org/10.1016/j.cirp.2020.04.072.

[99] B.A. Arnold, B.E. Bjarngard, J.C. Klopping, A modified pinhole camera method for investigation of X-ray tube focal spots, Phys. Med. Biol. 18 (4) (1973) 540–549, http://dx.doi.org/10.1088/0031-9155/18/4/006.

[100] J.M. Boone, Determination of the presampled MTF in computed tomography, Med. Phys. 28 (3) (2001) 356–360, http://dx.doi.org/10.1118/1.1350438.

[101] G. Di Domenico, P. Cardarelli, A. Contillo, A. Taibi, M. Gambaccini, X-ray focal spot reconstruction by circular penumbra analysis - Application to digital radiography systems, Med. Phys. 43 (1) (2016) 294–302, http://dx.doi.org/10.1118/1.4938414.

[102] B.A. Bircher, F. Meli, A. Küng, A. Sofiienko, Traceable x-ray focal spot reconstruction by circular edge analysis: from sub-microfocus to mesofocus, Meas. Sci. Technol. 33 (7) (2022) 074005, http://dx.doi.org/10.1088/1361-6501/ac6225.

[103] W.H. Richardson, Bayesian-based iterative method of image restoration*, J. Opt. Soc. Am. 62 (1) (1972) 55–59, http://dx.doi.org/10.1364/JOSA.62.000055.

[104] L.B. Lucy, An iterative technique for the rectification of observed distributions, Astron. J. 79 (6) (1974) 745, http://dx.doi.org/10.1086/111605.

[105] E. Shaked, S. Dolui, O.V. Michailovich, Regularized richardson-lucy algorithm for reconstruction of Poissonian medical images, in: 2011 IEEE International Symposium on Biomedical Imaging: From Nano To Macro, IEEE, 2011, pp. 1754–1757, http://dx.doi.org/10.1109/ISBI.2011.5872745.

[106] M. Engelhardt, J. Baumann, Determination of Size and Intensity Distribution of the Focal Spot of a Microfocus X-ray Tube Using Image Processing, Ecndt Th.2.5.4 (2006) 1–13.

[107] J.A. Nelder, R. Mead, A Simplex Method for Function Minimization, Comput. J. 7 (4) (1965) 308–313, http://dx.doi.org/10.1093/comjnl/7.4.308.

[108] Y. Wang, J. Yang, W. Yin, Y. Zhang, A new alternating minimization algorithm for total variation image reconstruction, SIAM J. Imaging Sci. 1 (3) (2008) 248–272, http://dx.doi.org/10.1137/080724265.

[109] A. Leclaire, L. Moisan, No-Reference Image Quality Assessment and Blind Deblurring with Sharpness Metrics Exploiting Fourier Phase Information, J. Math. Imaging Vision 52 (1) (2015) 145–172, http://dx.doi.org/10.1007/s10851-015-0560-5.

[110] M. Westsik, J.T. Wells, Y. Chahid, K. Morris, M. Milanova, M. Beardsley, M. Harris, L. Ward, S.G. Alcock, I.-T. Nistea, S. Cottarelli, S. Tammas-Williams, C. Atkins, From design to evaluation of an additively manufactured, lightweight, deployable mirror for Earth observation, in: T.B. Hull, D. Kim, P. Hallibert (Eds.), in: Astronomical Optics: Design, Manufacture, and Test of Space and Ground Systems IV, vol. 12677, International Society for Optics and Photonics. SPIE, 2023, 1267704, http://dx.doi.org/10.1117/12.2677303.

[111] N. Brierley, B. Nye, J. McGuinness, Mapping the spatial performance variability of an X-ray computed tomography inspection, NDT E Int. 107 (2019) 102127, http://dx.doi.org/10.1016/j.ndteint.2019.102127.

[112] M. Reiter, D. Weiß, C. Gusenbauer, M. Erler, C. Kuhn, S. Kasper, J. Kastner, Evaluation of a histogram-based image quality measure for X-ray computed tomography, in: 5th Conference on Industrial Computed Tomography, ICT, Wels, Austria, 2014, pp. 273–282.

[113] A. Obaton, Y. Gaillard, P. Bouvet, O. Guiraud, S. Genot, L. Gay, Evaluation of XCT image quality, in: 12th Conference on Industrial Computed Tomography, ICT, Furth, Germany, 2023, http://dx.doi.org/10.58286/27712.